JGR Space Physics

RESEARCH ARTICLE
10.1029/2021JA029466

Heppa III Intercomparison Experiment on Electron Precipitation Impacts: 2. Model-Measurement Intercomparison of Nitric Oxide (NO) During a Geomagnetic Storm in April 2010

M. Sinnhuber[1], H. Nesse Tyssøy[2], T. Asikainen[3], S. Bender[4,2], B. Funke[5], K. Hendrickx[6], J. M. Pettit[7], T. Reddmann[1], E. Rozanov[8,9], H. Schmidt[10], C. Smith-Johnsen[2], T. Sukhodolov[8,9,11], M. E. Szeląg[12], M. van de Kamp[12], P. T. Verronen[3,12], J. M. Wissing[13], and O. S. Yakovchuk[9,13,14]

[1]Karlsruhe Institute of Technology, Leopoldshafen, Germany, [2]Department Physics and Technology, Birkeland Centre for Space Science, University of Bergen, Bergen, Norway, [3]University of Oulu, Oulu, Finland, [4]Norwegian University of Science and Technology, Trondheim, Norway, [5]Instituto de Astrofísica de Andalucía, CSIC, Granada, Spain, [6]Formerly at the Department of Meteorology, Stockholm University, Stockholm, Sweden, [7]LASP, University of Colorado, Boulder, CO, USA, [8]PMOD/WRC, Davos and IAC ETH, Zurich, Switzerland, [9]Saint Petersburg State University, Saint Petersburg, Russia, [10]Max-Planck Institute for Meteorologie, Hamburg, Germany, [11]Institute of Meteorology and Climatology, University of Natural Resources and Life Sciences, Vienna, Austria, [12]Space and Earth Observation Centre, Finnish Meteorological Institute, Helsinki, Finland, [13]University of Rostock, Rostock, Germany, [14]Skobeltsyn Institute of Nuclear Physics, Lomonosov Moscow State University, Moscow, Russia

Abstract Precipitating auroral and radiation belt electrons are considered to play an important part in the natural forcing of the middle atmosphere with a possible impact on the climate system. Recent studies suggest that this forcing is underestimated in current chemistry-climate models. The HEPPA III intercomparison experiment is a collective effort to address this point.

In this study, we apply electron ionization rates from three data-sets in four chemistry-climate models during a geomagnetically active period in April 2010. Results are evaluated by comparison with observations of nitric oxide (NO) in the mesosphere and lower thermosphere. Differences between the ionization rate data-sets have been assessed in a companion study. In the lower thermosphere, NO densities differ by up to one order of magnitude between models using the same ionization rate data-sets due to differences in the treatment of NO formation, model climatology, and model top height. However, a good agreement in the spatial and temporal variability of NO with observations lends confidence that the electron ionization is represented well above 80 km. In the mesosphere, the averages of model results from all chemistry-climate models differ consistently with the differences in the ionization-rate data-sets, but are within the spread of the observations, so no clear assessment on their comparative validity can be provided. However, observed enhanced amounts of NO in the mid-mesosphere below 70 km suggest a relevant contribution of the high-energy tail of the electron distribution to the hemispheric NO budget during and after the geomagnetic storm on April 6.

1. Introduction

Energetic particles from the Sun or the terrestrial magnetosphere precipitate into the atmosphere at high geomagnetic latitudes. Due to magnetospheric shielding, protons from solar coronal mass ejections can mainly precipitate into the atmosphere inside the polar caps polewards of ~60° geomagnetic latitude. Electrons accelerated in the magnetotail to energies ranging from a few keV to hundreds of keV in auroral substorms precipitate in the auroral region. Electrons trapped in the outer radiation belt can be accelerated to energies from a few tens of keV to several MeV in geomagnetic storms initiated by solar coronal mass ejections or high-speed solar wind streams, and precipitate at mid-to-high latitudes, equatorwards of the auroral ovals (see review and references in Mironova et al. [2015]; Sinnhuber & Funke [2019]). The penetration depth of the precipitating particles depends on their energies, with auroral electrons mainly affecting the lower thermosphere above ~90 km, radiation belt electrons precipitating further down into the middle atmosphere, even into the upper stratosphere (1 MeV electrons to ≈50 km, e.g. Fang et al. [2010]).

This article is a companion to Nesse Tyssøy et al (2021), https://doi.org./10.1029/2021JA029128.

Key Points:

- Differences between multi-model mean results at high latitudes are consistent with differences in the ionization rate data-sets used
- Electron precipitation above 80 km is well reproduced for all ionization rate data-sets despite large differences between individual CCMs
- Anisotropic precipitation from ≥300 keV electrons could provide up to 0.05–0.15 Gmol NO per hemisphere in storm main and recovery phase

Correspondence to:

M. Sinnhuber,
miriam.sinnhuber@kit.edu

Citation:

Sinnhuber, M., Nesse Tyssøy, H., Asikainen, T., Bender, S., Funke, B., Hendrickx, K., et al. (2022). Heppa III intercomparison experiment on electron precipitation impacts: 2. Model-measurement intercomparison of nitric oxide (NO) during a geomagnetic storm in April 2010. *Journal of Geophysical Research: Space Physics*, *127*, e2021JA029466. https://doi.org/10.1029/2021JA029466

Received 21 APR 2021
Accepted 19 NOV 2021

Collisions of precipitating particles with the most abundant air molecules and atoms N_2, O_2 and O lead to the formation of primary ions N_2^+, O_2^+, O^+, N^+ as well as to excited and ground-state neutral dissociation products (N^4S, N*, $O(^3P)$, $O(^1D)$). Reactions of nitrogen atoms in the ground and excited states lead to formation of NO via the reaction

$$N + O_2 \rightarrow NO + O. \quad (1)$$

This reaction is much faster for the excited states of N at the prevailing low temperatures in the middle atmosphere, but the pronounced temperature dependence of the reaction involving ground state nitrogen favors NO production at higher thermospheric temperatures, leading to a significantly larger equilibrium concentration of NO at temperatures ≥400 K (e.g., Sinnhuber & Funke [2019]). Charge exchange and subsequent ion-neutral and ion-ion reactions also contribute to NO formation (Sinnhuber et al., 2012; Verronen & Lehmann, 2013). During the daytime, electromagnetic radiation in the extreme UV (EUV) and soft x-ray wavelength range causes photoinization, which leads to the same chain of reactions forming NO, though the distribution of primary ions depends on the EUV spectrum. During geomagnetic storms and auroral substorms, particle impact ionization is dominated by auroral and radiation belt electrons, with a smaller contribution of *soft* protons (Yakovchuk & Wissing, 2019). To relate the ionization rate to the rate of NO formation, chemistry-climate models often use a well established relation of 1.25 NOx formed by one ionpair based on (Jackman et al., 2005; Porter et al., 1976). This approach yields in general a good agreement with observations of the chemical impact for large solar proton events below 80 km (Funke et al., 2011; Jackman et al., 2001). A more sophisticated approach is to model the ion chemistry in detail; this approach has been used successfully in the lower thermosphere where only five ions (O_2^+, N_2^+, O^+, NO^+, N^+) and some excited species need to be taken into consideration, and it has also been used in models of mesospheric and stratospheric ion chemistry, for example, in one-dimensional models like SIC or UBIC (Verronen et al., 2005; Winkler et al., 2008). Recently, detailed D-region ion chemistry schemes have been developed for global models as well (Andersson et al., 2016; Egorova et al., 2011; Verronen et al., 2016).

NOx produced by energetic electron precipitation in the mesosphere and lower thermosphere is very long-lived during polar night and is transported down into the stratosphere around 25 km in most polar winters (Funke et al., 2014; WMO, 2018). As NOx contributes to catalytic ozone loss in the upper stratosphere, these geomagnetically modulated NOx intrusions lead to ozone loss and changes in the radiative balance of the upper stratosphere varying from year to year (Sinnhuber et al., 2018). Energetic electron precipitation into the mesosphere and lower thermosphere thus initiate a chemical-dynamical coupling mechanism that potentially impacts atmospheric dynamics down to regional weather systems at mid-and high latitudes (Arsenovic et al., 2016; Asikainen et al., 2020; Maliniemi et al., 2014, 2019; Seppälä et al., 2009). This so-called *geomagnetic forcing* is considered as a potential contributor to the natural variability of the climate system, and recommended to be included in ongoing and future chemistry-climate model projections, for example, for the CMIP6 experiments (Matthes et al., 2017). The latter recommendations by Matthes et al. (2017) include a parameterization of the medium-energy electron (MEE, ≥30 keV) ionization which is based on POES/MEPED electron flux observations (APEEP, see van de Kamp et al. [2016]). Ionization by MEEs with their penetration directly into the middle atmosphere could be especially important for the coupling to the dynamics. However, recent studies suggest a systematic underestimation of the electron fluxes and ionization rates particularly during and after geomagnetic storms by APEEP (Mironova et al., 2019; Nesse Tyssøy et al., 2019) as well as by other ionization rate data-sets based on POES/MEPED electron flux observations (Pettit et al., 2019; Smith-Johnsen et al., 2017).

The HEPPA III intercomparison experiment is a collective effort to address this issue. This study is the second of two papers dealing with the evaluation of the electron precipitation impact on the atmosphere. In the first paper, eight different ionization rate data-set. all using POES/MEPED data were compared for a geomagnetically disturbed period in April 2010, and their differences were analyzed in detail (Nesse Tyssøy et al., 2021). A main result of the first paper is that ionization rates differ by up to an order of magnitude as well as in their penetration depths depending on the choices made in their derivation even when using the same data-set of electron fluxes. Here, we investigate the respective atmospheric impact of these ionization rates and their spread by analyzing results from chemistry-climate models driven by three of these ionization rate data-sets for the same period of time in April 2010. To account for the large differences between ionization rates, we choose three data-sets that represent the full range of the spread discussed in Nesse Tyssøy et al. (2021). To evaluate the model response, results of the model experiments are compared with satellite observations of nitric oxide (NO) from three instruments complementary in vertical, spatial, and temporal coverage (SOFIE/AIM as well as MIPAS and SCIAMACHY on

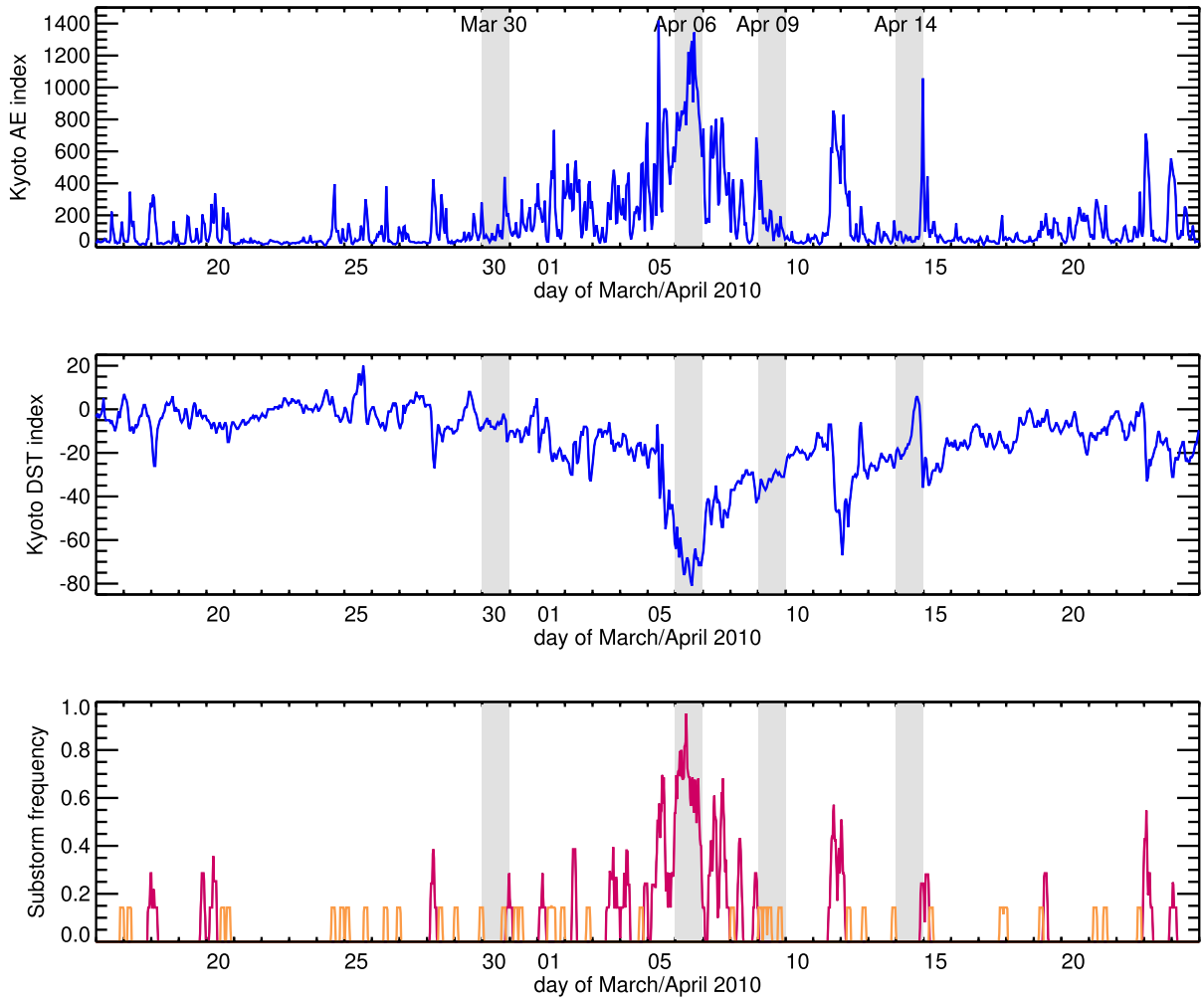

Figure 1. Hourly AE index (upper panel), hourly DST index (middle panel) and frequency of isolated (orange) and non-isolated (red) substorms (lower panel) from 16 March to 24 April 2010. Highlighted by gray shading are March 30, April 6, April 9 and April 14, see also dates provided at top of figure. The frequency of substorms is calculated based on a 24-hr moving average, with the substorm duration assumed to be 30 min. The substorm onsets are derived following Newell and Gjerloev (2011b) based on the SML index, an improved version of the traditional AE index (Newell & Gjerloev, 2011a). Isolated substorm onsets are separated by at least 3 hr.

ENVISAT). NO was chosen as a diagnostic because high-latitude NO abundances in the mesosphere and lower thermosphere are assumed to be dominated by particle impact ionization (Barth et al., 2003; Marsh et al., 2004; Sinnhuber et al., 2016). We use four different *high-top* coupled chemistry-climate models extending into the lower thermosphere to evaluate the electron ionization rate data-sets in the mesosphere and lower thermosphere. Model runs are carried out covering the same period of enhanced geomagnetic activity in April 2010 already described by Smith-Johnsen et al. (2018) and in the companion paper, Nesse Tyssøy et al. (2021). This period follows a geomagnetically very quiet period in early 2010. It is characterized by an increase in geomagnetic activity starting on 30 March 2010 with an enhanced substorm activity peak. Geomagnetic activity is largest during a geomagnetic storm onset on April 5 and 6 (see Figure 1), which was initiated by a solar coronal mass ejection but was not accompanied by a solar proton event. Kp values of 8 are reached during April 5, and the daily mean Ap is 55 on April 5, 44 on April 6.

The models and data-sets used are introduced in Section 2, ionization rate data-sets in Section 2.1, chemistry-climate models in Section 2.2, satellite data-sets in Section 2.3. The model-measurement intercomparison is shown in Section 3, a discussion evaluating the applicability of the different ionization rate data-sets is provided in Section 3.3, and an estimate for the contribution of auroral electrons and MEE to the hemispheric NO budgets during this event is given in Section 3.4.

2. Characterization of Data-Sets and Models

In this section, the data-sets and models used for the intercomparison are described and their uncertainties and variability are characterized.

2.1. Ionization Rate Data-Sets

Three ionization rate data-sets are used here, AIMOS (see Section 2.1.1), APEEP (see Section 2.1.2), and OULU (see Section 2.1.3) described in detail in the companion paper, Nesse Tyssøy et al. (2021). In all three data-sets, ionization due to medium-energy electron (MEE, ≥30 keV) precipitation is based on observations of electron fluxes from the MEPED instruments on the NOAA POES and EUMETSAT MetOP satellites. These instruments record the MEE flux in the bounce loss cone in three energy ranges: >30 keV, >100 keV and >300 keV. The ionization rate data-sets differ in their use of either one or two of the directional telescopes, in the treatment of instrument-related problems, the spectral and spatial interpolation of the electron fluxes, the electron energy range, and the energy deposition algorithm. The three data-sets were chosen because of these differences, to provide typical examples of different data preparation methods and to span the full range of ionization rates from the larger group of eight ionization rate data-sets compared in Nesse Tyssøy et al. (2021). A comparison of zonally averaged daily ionization rates from the data-sets is provided for four days in Section 2.1.4.

2.1.1. AIMOS

The Atmospheric Ionization Module Osnabrück *AIMOS* v1.6 (Wissing & Kallenrode, 2009) provides 3-D ionization rates due to protons, auroral, and MEE electrons in the range 0.154–300 keV and alpha particles with a two-hourly resolution for the time-period 2001–2012 on a geographic latitude/longitude grid.

AIMOS uses both TED and MEPED data from the 0° detectors. Since the MEPED channels have no upper energy limit, MEPED electron fluxes are converted into differential channels by subtracting the upper from the lower channels, resulting in the bands 30–100 keV and 100–300 keV. Contamination of the electron channels by high-energy proton precipitation is removed by neglecting the MEPED electron channels if the omni-directional proton channel P7 sensitive to ≥35 MeV protons (Evans & Greer, 2006) shows more than 2 counts. This effectively cuts out MEE precipitation during solar proton events and in the South Atlantic Anomaly. The most recently launched set of satellites are used in AIMOS. For the selected period these are POES 17 covering the morning/evening sector and POES 18 covering the day/night sector. Mean flux maps have been calculated based on 8 years of satellite data (2002–2009) grouped by Kp level, geographic location with a 3.75° latitude/longitude resolution, and 6-hr sectors of magnetic local time (MLT). For the mean of every bin the upper and lower 25% of the data have been neglected which reduces noise and outliers while preserving the spatial pattern. Thus each flux map represents the typical spatial precipitation pattern of a single channel on a global map while preserving variations in four MLT sectors. These maps are then scaled to the observed flux conditions in every two-hour interval. Only the regions with high fluxes (i.e., within the auroral oval) are used for scaling to reduce the impact of noise in the real time data. Bins with similar energy-flux spectra are grouped together resulting in 42 regions for each time interval that is processed further. Proton, electron and α particle fluxes are fitted by a multiple power-law fit as a function of energy with up to 5 fits with variable intersections (see Wissing et al. [2016]). Each of these particle spectra is then convolved with the ionization profiles resulting from a Monte Carlo simulation of the particle incidents into an atmospheric detector using the GEANT4 toolkit (Agostinelli et al., 2003). The atmospheric detector is similar to Schröter et al. (2006) but atmospheric parameters have been taken from the HAMMONIA model (Schmidt et al., 2006) and the NRLMSISE-00 model (Picone et al., 2002). The AIMOS model is available at http://www.ionization.de.

2.1.2. APEEP

The APEEP precipitation model (van de Kamp et al., 2016) provides daily ionization rates for medium-energy electron precipitation parameterized by the geomagnetic *Ap* index on a geomagnetic latitude grid, considering electrons with energies from 30 keV to 1 MeV.

APEEP uses MEPED data of the 0° detectors measured during the years 2002–2012. The electron data were corrected for proton contamination using measurements from the MEPED P7 proton flux detector, similar to the approach used for AIMOS. Time periods of solar proton events were removed from the database. To avoid noise contamination, all data points where the electron flux of the >30 keV channel was lower than

250 electrons/cm^{2}sr s were replaced by zeros, keeping in mind that this might cause an underestimation of low fluxes, requiring additional steps which we describe below. All available flux data in each of the three channels were binned dependent on IGRF L shell at a resolution of 0.5, and a temporal resolution of 1 day, and averaged over each bin. For each day of data and each value of L, a spectrum model was fitted to the measured fluxes in the three different energy ranges which assumes a power-law decrease of spectral density with energy between 30 keV and 1 MeV. The output of this procedure is expressed in the spectral gradient k and the flux >30 keV F_{30} resulting from the fit, for each day and each L. Medians of the daily values of F_{30} and k over the period 2002–2012 were calculated for each value of L, and for a range of bins of the concurrent magnetic index Ap. Analytical expressions were fitted to these median values, giving a model dependent on only Ap and L-value. In these expressions, the dependence on L was expressed as dependent on the distance from the location of the plasmapause, which was modeled following O'Brien and Moldwin (2003). Low anomalies of the flux from these fitted curves near or below the noise floor were considered to be due to the noise-removal measure and ignored. The model is meant to give *typical* expected flux spectra from the daily Ap value. The resulting precipitation flux spectra are used to calculate atmospheric ionization using the parameterization of electron impact ionization by Fang et al. (2010) and a representation of the atmosphere, as for example, the NRLMSISE-00 model (Picone et al., 2002). This model was used in the recommendation for the CMIP-6 forcing data set (Matthes et al., 2017). Data are available, for example, on the Webpage of the SPARC SOLARIS-HEPPA project https://solarisheppa.geomar.de/cmip6 for the period 1850–2300, where the data from 2015 onward (the future at the time of preparing this dataset) are based on the Solar Reference Scenario.

2.1.3. OULU

The University of Oulu data-set (called OULU in the following) provides daily ionization rates for medium-energy electron precipitation on a geomagnetic latitude grid for the period 1979-present considering electron energies of 30 keV to 1 MeV.

OULU uses the logarithmic average of electron flux data from the MEPED 0° and 90° telescopes, see (Nesse Tyssøy et al., 2021). Electron flux measurements have been corrected for low energy proton contamination using the POES proton data which in turn have first been corrected for radiation damage severely affecting the detectors after a few years (Asikainen et al., 2012; Asikainen & Mursula, 2011). Electron flux measurements have further been corrected for non-ideal energy dependent detector efficiency (Asikainen & Mursula, 2013), and errors in the satellite position data have been fixed using a set of recalculated auxiliary data dependent on satellite position (Asikainen, 2017). This corrected POES data-set was recently used to construct a spatially and temporally homogeneous composite record of daily energetic electron fluxes from 1979 to the present (Asikainen, 2019; Asikainen & Ruopsa, 2019). It accounts for the changing background noise related to cosmic rays, compensates for the changing measurement location of POES satellites and scales the measurements of older SEM-1 (before 1998) and newer SEM-2 (after 1998) detectors to the same level. Electron flux data are provided in three integral energy channels corresponding to the three MEPED electron energy channels in the dawn (roughly 7 hr MLT) and dusk (19 hr MLT) sectors in 2°-bins of corrected geomagnetic latitude. The fluxes in the two opposite MLT sectors are averaged, and the integral energy spectrum of precipitating electrons is expressed as a power-law spectrum determined by the three integral energy channels between 30 keV and 1 MeV. The corresponding differential spectrum is numerically estimated with 10 keV spacing by differentiating the integral spectrum. The atmospheric ionization profile is computed using the parameterization by Fang et al. (2010) and a background atmosphere provided by the NRLMSISE-00 model (Picone et al., 2002).

2.1.4. Comparison of Ionization Rate Data-Sets

A comparison of daily averaged zonally averaged ionization rates from the AIMOS, APEEP, and OULU data-sets covering the mesosphere and lowermost thermosphere (1 hPa to 10^{-4} hPa, ≈45–105 km) is provided in Figure 2. Shown are results for a quiet day before the increase of geomagnetic activity, during the storm main phase, during the recovery phase, and at the end of the period of geomagnetic activity. To account for the low-energy cut-off of APEEP and OULU, the auroral low energy ionization has been complemented by AIMOS data considering only electrons <30 keV. Thus above ≈0.000 5 hPa (blue dashed lines in Figure 2), the ionization rates are nearly identical. At higher pressure levels, the three data-sets differ systematically in their latitudinal extent, vertical coverage, intensity, and temporal evolution throughout the storm phases. Because their electron energies are limited to <300 keV, the AIMOS data do not extend as far down into the mesosphere as the other two data-sets. Ionization rates from the AIMOS and OULU data-sets show elevated ionization levels throughout their complete nominal

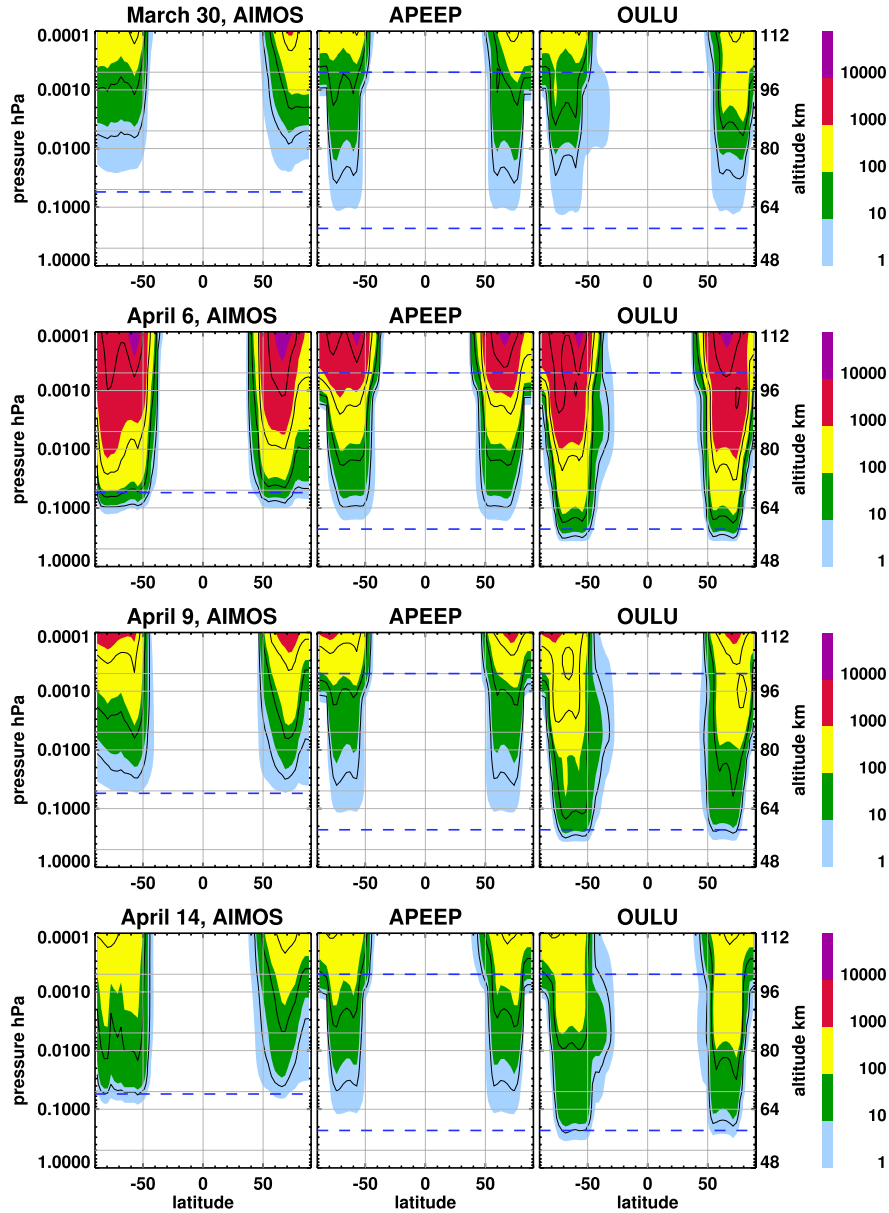

Figure 2. Comparison of daily mean, zonal mean ionization rates ($cm^{-3}s^{-1}$) from the three ionization rate data-sets (from left to right) AIMOS, APEEP, and OULU. All data are gridded to the spatial grid of the EMAC model. From top to bottom: 30 March 2010 representing the quiet background before the storm; 6 April 2010, representing the storm main phase; 9 April 2010 representing the recovery phase of the geomagnetic storm; 14 April 2010, at the end of the period of enhanced geomagnetic activity. Black lines mark contour intervals of 5, 50, 500, and 5,000 $cm^{-3}s^{-1}$. Gray lines mark −50°, 0° and 90° and 0.5, 0.1, 0.05, 0.01, 0.005, 0.001, and 0.0005 hPa. Dashed blue lines mark the approximate range of validity of the data-sets based on the electron energies considered. The altitudes provided on the right-hand axis are approximative, based on a scale width of 8 km.

pressure range particularly during days of enhanced geomagnetic activity (April 6, 9, and 14), but the ionization rates from the APEEP data-set never reach the nominal lower altitude limit of ≈0.23 hPa.

During the quiet period before the storm onset (March 30), enhanced values of ≥10 $cm^{-3}s^{-1}$ extend down to 0.05 hPa in AIMOS, down to about 0.1 hPa in APEEP and OULU. During the storm main phase (April 6), strongly enhanced values of more than 1,000 $cm^{-3}s^{-1}$ extend further down in AIMOS and OULU (about 0.01 hPa) than in APEEP (about 0.001 hPa). Moderately enhanced values of ≥10 $cm^{-3}s^{-1}$ reach down to 0.23 hPa in OULU, but only down to about 0.05 hPa in AIMOS and OULU; at 0.1 hPa OULU data are two orders of magnitude larger

Table 1
Features of the Four Chemistry-Climate Models Used in the Intercomparison Experiment

Model	WACCM	HAMMONIA	EMAC	KASIMA
Top altitude	140 km	220 km	220 km	120 km
Vertical levels	88	119	74	63
Horizontal res.	0.95° × 1.25°	1.9° × 1.9°	2.8° × 2.8°	2.8° × 2.8°
Thermospheric	Full D-region	5 pos. ions	5 pos. ions	const. N, NO
ion chemistry	NO UBC[a]			NO UBC
Mesospheric i.c.	Full D-region	const. N, NO	5 pos. ions	const. N, NO
Ionization by:	e^-, p^+[b]	e^-, p^+, α	e^-, p^+, α	e^-, p^+, α
Photoionization	para[c]	para[c]	para[c]	simple low

[a]Upper Boundary Condition. [b]WACCM includes Solar Protons only, all others include Soft and Solar Protons. [c]Parameterization of EUV photoionization rates by Solomon and Qian (2005).

than AIMOS data as the extended range in AIMOS is due to bremsstrahlung. Enhanced ionization rates from the AIMOS model extend further into the polar cap regions in the upper mesosphere (0.05–0.001 hPa) than in the other data-sets especially in the Southern hemisphere, indicating a less well confined auroral oval. In the recovery phase and at the end of the period of enhanced geomagnetic activity (April 9 and 14), AIMOS and APEEP rates have nearly recovered to background values, while enhanced ionization rates of 10–500 $cm^{-3}s^{-1}$ persist throughout most of the mesosphere (0.3–0.001 hPa) in the OULU model until at least April 14 due to the more anisotropic pitch angle distribution after the storm captured only by the 90° detector of the POES/MEPED instrument. This is shown in more detail in the companion paper Nesse Tyssøy et al. (2021), see their Figure 4, where it is shown that precipitation in OULU in the high-energy tail of the MEE distribution (≥300 keV) continues until April 11, until April 14 in the MEE range of ≈100–300 keV.

2.2. Chemistry-Climate Models

Results from four chemistry-climate models are used: WACCM (Section 2.2.1), HAMMONIA (Section 2.2.2), EMAC (Section 2.2.4), and KASIMA (Section 2.2.4). All four models are *high-top* models extending into the lower thermosphere (≥115 km). All models use externally prescribed ionization rate data for medium-energy electron ionization and either internally calculated or prescribed auroral electron ionization as well as a parameterization of EUV photoionization. For this study, all model experiments are carried out in the *specified dynamics* mode, nudging temperatures and wind fields to meteorological analyses data in the troposphere and stratosphere. A comparison of the most relevant features of the four models as used here is given in Table 1.

2.2.1. Whole Atmosphere Community Climate

The Whole Atmosphere Community Climate Model *WACCM* is the atmospheric part of the Coupled Earth System Model *CESM*. The WACCM version 6 used here is described in detail by Gettelman et al. (2019). The vertical extent of WACCM is from the Earth's surface to 6×10^{-6} hPa (≈ 140 km). Here we use the specified dynamics mode with 88 pressure layers. The horizontal resolution is 0.95° × 1.25° in latitude×longitude. Temperatures and winds below ≈50 km are taken from the MERRA2 reanalysis data (Molod et al., 2015). The orographic gravity wave scheme has been updated recently and incorporates near-surface nonlinear drag processes following Scinocca and McFarlane (2000) as well as a feature-based algorithm to derive forcing data based on Bacmeister et al. (1994). A non-orographic gravity wave drag parameterization is used following Richter et al. (2010) with a separate specification of frontal and convective gravity wave sources. Here we use a chemical mechanism appropriate for the middle atmosphere with a reduced set of tropospheric reactions. Overall, the scheme of chemical reactions has evolved from previous versions (e.g., Emmons et al.,2010; Kinnison et al., 2007; Lamarque et al., 2012; Marsh et al., 2013; Tilmes et al., 2016). The reaction rate coefficients have been updated following the JPL 2015 recommendations (Burkholder et al., 2015). Additional D-region ion chemistry considering 307 reactions of 20 positive ions and 21 negative ions is included as an extended representation for the chemical impacts of energetic particle precipitation (Andersson et al., 2016; Verronen et al., 2016); this scheme replaces the parameterized HO_x and NO_x production used in previous model versions.

For photoionization and heating rates at wavelengths shorter than Lyman-α, the F10.7 based parameterization of Solomon and Qian (2005) is used. Atmospheric ionization by solar protons is included based on observed proton fluxes in the energy range of 1–300 MeV from the geostationary GOES satellites (Jackman et al., 2011). Ionization by auroral electrons is described by an internally generated aurora based on the daily variation of the hemispheric power which is related to the Kp index following Zhang and Paxton (2008), assuming a Maxwellian distribution with a fixed characteristic energy of 2 keV (Marsh et al., 2007; Roble & Ridley, 1994). Ionization by medium-energy electrons is prescribed by the ionization rate data-sets introduced in Sect. 2.1. For APEEP and OULU, the contributions of MEE electrons and the internally generated aurora are added up, for AIMOS, the internal aurora is replaced by AIMOS data. In addition, WACCM also contains an upper boundary condition (UBC) for NO, prescribing NO in the uppermost model box by the NOEM empirical model (Marsh et al., 2004). NOEM and thus the UBC vary with solar radio flux (F10.7) and geomagnetic activity (Kp).

2.2.2. Hamburg Model for the Neutral and Ionized Atmosphere

The Hamburg Model for the Neutral and Ionized Atmosphere *HAMMONIA* is a revised version of the general atmospheric circulation model *ECHAM5* (Roeckner et al., 2006), in which the upper boundary is raised to ≈200–250 km ($1.7e^{-7}$ hPa). A detailed description of the model can be found in (Meraner et al., 2016; Schmidt et al., 2006). The model contains 119 vertical levels with a thickness varying from 600 m in the upper troposphere to 3 km in the mesosphere and 8 km in the thermosphere. In the model, the system of hydro-thermodynamic equations is solved by the spectral method with triangular truncation T63, which corresponds to a horizontal resolution of approximately 1.9° × 1.9° in latitude and longitude. Here we use the model in specified dynamics mode, assimilating ECMWF ERA interim data up to 1 hPa. Orographic and non-orographic gravity wave parameterizations follow the approaches of Lott and Miller (1997) and Hines (1997), respectively. Parameters of the gravity wave parameterizations were set to the "weak background" scenario of Meraner et al. (2016) which allows for a reasonable representation of the mesosphere/lower thermosphere (MLT). For the proper description of the thermospheric processes, the model was extended to include radiative heating due to the absorption of extreme solar ultraviolet radiation, cooling due to infrared radiation in case of local thermodynamic equilibrium violation, molecular diffusion, Joule heating, and ion drag (Schmidt et al., 2006). HAMMONIA includes the MOZART3 package to describe atmospheric chemistry (Kinnison et al., 2007). The calculation of the NO photodissociation rate is based on Minschwaner and Siskind (1993) and includes the NO slant column, which allows taking into account the self-absorption by the extinction of solar light by NO in the upper layers.

Ionization rates from auroral electrons, auroral and solar protons as well as heavier ions are provided by the AIMOS data-set. Electron ionization rates from medium-energy electrons are provided by data from the ionization rate data-sets AIMOS, APEEP, or OULU. For APEEP and OULU, auroral electron precipitation is taken from the AIMOS data-set using a cut-off energy of 30 keV. Photoionization is parameterized according to Solomon and Qian (2005) as an additional source of NO in the thermosphere. The chemical module was supplemented by the 5-ion (O^+, O_2^+, M^+, N_2^+, NO^+) chemistry in the thermosphere (Kieser et al., 2009) and by the parameterization of NO_x and HO_x production by energetic particles in the middle atmosphere (Jackman et al., 2005) below ≈90 km.

2.2.3. ECHAM/MESSy Atmospheric Chemistry

The ECHAM/MESSy Atmospheric Chemistry model *EMAC* is atmospheric chemistry and climate simulation system that includes sub-models describing a wide range of atmospheric processes (Joeckel et al., 2010). EMAC uses the second version of the Modular Earth Submodel System (MESSy2) to link multi-institutional computer codes. The core atmospheric model is ECHAM5 (Roeckner et al., 2006). For the present study, we used ECHAM5 version 5.3.02 and MESSy version 2.53.2 in the *upper atmosphere* mode with 74 vertical layers and a model top height of ≈220 km ($3e^{-7}$ hPa, EMAC submodule EDITH). Joule heating and ion drag are considered following Hong and Lindzen (1976) but scaled by the geomagnetic Kp index; molecular diffusion has been implemented following Schmidt et al. (2006). The horizontal resolution is T42, corresponding to a resolution of about 2.8° × 2.8° in latitude and longitude. The model is nudged to the ECMWF ERA interim reanalysis data from the surface up to 1 hPa with decreasing nudging strength in a transition region in the six levels above. For orographic gravity waves, the parameterization of Lott and Miller (1997) is used, for non-orographic gravity waves, the Hines parameterization is used (Hines, 1997) using the same setting as in HAMMONIA (see Section 2.2.2). Submodules RAD and RAD-FUBRAD are used for radiative heating and cooling rates (Dietmüller et al., 2016; Roeckner et al., 2003), using the wavelength grid provided by FUBRAD for UV radiative heating in the upper mesosphere and thermosphere (Kunze et al., 2014; Nissen et al., 2007). For gas-phase reactions,

Table 2
Overview Over Model Experiments Carried Out for This Study and Some of Their Distinguishing Properties

Name	MEE	Aurora	Other	UBC
AIMOS	AIMOS	AIMOS	p^+[b], α[c], EUV[d]	yes[e]
APEEP	APEEP	AIMOS/internal[a]	p^+, α, EUV	Yes
OULU	OULU	AIMOS/internal	p^+, α, EUV	Yes
Sens1	AIMOS	None	p^+, α, EUV	Yes
Sens2	None	AIMOS	p^+, α, EUV	Yes
Sens3	AIMOS	None	p^+, α	Yes
Sens4	AIMOS	None	None	Yes
Sens5	AIMOS	None	p^+, EUV	none
Sens6	AIMOS	None	EUV	none

Note. For the sensitivity experiments, MEE and auroral electrons are separated by cutting the rates above or below 0.01 hPa (WACCM, HAMMONIA, EMAC) respectively 80 km (KASIMA).

[a]either AIMOS with cut-off energies at 30 keV (HAMMONIA, EMAC, KASIMA) or the internally generated aurora (WACCM). [b]solar protons in WACCM, solar and soft protons in HAMMONIA, EMAC and KASIMA. [c]He^+, only in HAMMONIA, EMAC and KASIMA. [d]EUV photoionization rates. [e]upper boundary conditions in WACCM and KASIMA. Sens3 and Sens4: HAMMONIA, EMAC, KASIMA. Sens5 and Sens6: WACCM.

the submodule MECCA is used (Sander, Baumgaertner, et al., 2011; Sander, Abbatt, et al., 2011), and photolysis rates are calculated with the JVAL submodule (Sander et al., 2014). For NO photolysis, the parameterization from Allen and Frederick (1982) is used without correction for self-absorption.

Particle impact ionization rates for auroral electrons, auroral and solar protons and heavier ions are provided by AIMOS data, medium-energy electrons are provided by AIMOS, APEEP, or OULU. For model experiments with APEEP and OULU rates, auroral electron precipitation is provided by results from the AIMOS model using cut-off energy of 30 keV. Photoionization rates are calculated based on the parameterization of Solomon and Qian (2005). A simple five-ion chemistry scheme is used to calculate the impact of particle impact and photoionization on the neutral composition, the primary ions are calculated based on the approach used in the 3dCTM model as described in Sinnhuber et al. (2018).

2.2.4. KArlsruhe SImulation Model of the Middle Atmosphere

The KArlsruhe SImulation Model of the middle Atmosphere *KASIMA* is a three-dimensional mechanistic model of the middle atmosphere solving the primitive equations in spectral form. For the simulations presented here, 63 vertical layers are used between 300 hPa and the model top pressure at 3.6×10^{-5} hPa (≈120 km). The horizontal resolution is about 2.8° × 2.8°. The model is run in the specified dynamics mode and applies temperatures, vorticity, and divergence below approximately 1 hPa together with the geopotential at the lower boundary from the ERA INTERIM reanalysis data set. KASIMA uses parameterizations for radiative heating and cooling and a gravity wave drag scheme and includes middle atmosphere neutral chemistry. A detailed description of the model including the physical parameterizations and the chemical solver is found in Kouker et al. (1999). Recent model updates are given in Sinnhuber et al. (2018). In addition, NO photolysis in 6 bands covering the Schumann-Runge continuum has been added. The diffusive flux of NO at the upper boundary is calculated using the linearly extrapolated value of the mixing ratio from below.

Particle impact ionization rates for auroral electrons, auroral and solar protons and heavier ions are provided by AIMOS data, medium-energy electrons are provided by AIMOS, APEEP, or OULU. For model experiments with APEEP and OULU rates, auroral electron precipitation is provided by results from the AIMOS data-set using cut-off energy of 30 keV. A small contribution of a photoionization source of 400 $cm^{-3}s^{-1}$ above 0.001 hPa serves as an upper boundary condition for the middle atmosphere outside the auroral zone. The impact of ionization on the neutral composition is considered by production rates of 0.55 N atoms, 1.15 O atoms, and 0.7 NO molecules per ion pair. For HOx, a pressure dependent efficiency is used following Jackman et al. (2005).

2.2.5. Modeling Strategy

Three core experiments and four sensitivity experiments were carried out with each chemistry-climate model, see overview in Table 2. All model experiments were run from 1 January 2010 until 30 April 2010, starting with an identical setting, apart from the prescribed and internally generated ionization rates and the setup of other NO sources which vary between model experiments. One core model experiment is carried out with the AIMOS, APEEP, and OULU ionization rate data-sets each. For the core experiments APEEP and OULU, auroral electron ionization is prescribed from AIMOS with cutoff energy at 30 keV for HAMMONIA, EMAC, and KASIMA, and from the internally generated aurora for WACCM. The sensitivity experiments were set up to quantify the contributions of different sources of NO to the overall NO amounts in the individual models. The electron ionization rates of the sensitivity model experiments are based on the AIMOS data-set because AIMOS provides ionization rates for auroral and MEE electrons, and therefore allows all chemistry-climate models to use identical auroral electron ionization rates. Different sources of NO in the mesosphere and lower thermosphere are subsequently switched off in such a way that the difference between the two model experiments contributes to one source of NO to the overall NO amount. The model experiments were designed to test the contributions of auroral electrons, MEE, photoionization (HAMMONIA, EMAC, and KASIMA), the NO upper boundary condition

(WACCM), and the proton ionization as outlined in Table 2. For all model experiments NO, temperature and geopotential altitude on the native pressure levels of the models are output on the footprints of the SOFIE, SCIAMACHY, and MIPAS satellite instruments (see Section 2.3) and subsequentially interpolated onto the altitude grids of the satellite data-sets.

2.2.6. Model-Model Intercomparison: NO and Temperature

In the following, results of NO and temperature from the AIMOS model experiment using all four chemistry-climate models are compared on the SCIAMACHY/MIPAS footprints to provide a common spatial and temporal sampling.

In Figure 3, a comparison of daily mean zonal mean daytime NO densities in the altitude range 50–115 km is shown on the SCIAMACHY footprint for four days: March 30, April 6, April 9, and April 14. The models show similar temporal variabilities, but substantial differences in the NO amount on all four days. These differences are particularly pronounced in the lower thermosphere above 90 km altitude at mid- and low latitudes. In this region, NO densities from KASIMA are lower than 1×10^7 cm^{-3}, between 7.5×10^7 cm^{-3} and 1×10^8 cm^{-3} in WACCM, and more than 1×10^8 cm^{-3} in HAMMONIA and EMAC, more than an order of magnitude higher than in KASIMA. This low-latitude thermospheric NO signal is presumably due to photoionization, which is calculated using the F10.7 based parameterization of Solomon and Qian (2005) in WACCM, HAMMONIA and EMAC, while a low constant value is used in KASIMA. In the high-latitude lower thermosphere, all models show enhanced values of NO varying in strength with geomagnetic activity. Again, absolute values are lowest in KASIMA during quiescent conditions (March 30), with the highest values in EMAC about an order of magnitude larger. During and after the geomagnetic storm on April 6, the lower thermospheric NO amounts are much higher than during the quiescent period in all models, with the highest values exceeding 4×10^8 cm^{-3} in HAMMONIA and EMAC, and values in KASIMA and WACCM about a factor of 4 lower. The systematic differences in the high-latitude lower thermosphere during the geomagnetic storm, between HAMMONIA and EMAC on the one hand, and WACCM and KASIMA on the other hand, could indicate an impact of NO from the mid-thermosphere above the top height of WACCM and KASIMA. The high-latitude NO peak broadens and extends further down into the mesosphere than during the quiescent period in all models, showing the impact of the geomagnetic storm down to at least 70 km in high Southern latitudes. The mesospheric NO enhancement is strongest during the event, and reaches down furthest, in WACCM, reaching down to below 70 km in the Southern hemisphere, down to 80 km in the Northern hemisphere. After the event (April 9 and April 14), the high-latitude NO enhancement is declining in all models both in the thermosphere and in the mesosphere, but elevated thermospheric NO densities persist in all models except WACCM until at least April 14. In the Southern hemisphere mesosphere, enhanced NO values persist and propagate downwards at least until April 9 in all models. Downward propagation is strongest and most persistent in WACCM, where enhanced values of more than 2.5×10^7 cm^{-3} of NO have reached altitudes below 65 km on April 14.

Since the reactions of NO production are highly dependent on temperature, differences in the temperatures between the models could contribute to the large differences in the NO response seen in the models as shown in Figure 3. Figure 4 provides a comparison of modeled temperatures in the mesosphere and lower thermosphere (50–115 km) for 30 March 2010, for three latitude regions: high Southern latitudes, tropics, and moderately high Northern latitudes. Results are provided on the footprints of the MIPAS daytime and nighttime data, and MIPAS temperatures are shown as well for reference. In the lower mesosphere below 70 km, results from all models agree reasonably well with each other and with the observations. In the uppermost mesosphere at 80–90 km, a vertical wave structure consistent with a tidal signal is observed which is most pronounced in the tropical region. This is reproduced but not fully resolved vertically in WACCM, HAMMONIA and EMAC, but does not appear in KASIMA. Above 90 km, EMAC significantly overestimates temperatures in all regions shown, with differences larger than 100 K at 115 km, indicating a systematic problem of the treatment of heating and cooling in the thermosphere in this model. Between 100 and 115 km in most latitudes, the temperatures in EMAC exceed the threshold of thermal NO formation around 400 K, indicating that thermal NO production could contribute to the very high amounts of thermospheric NO in the EMAC model during quiescent times. However, KASIMA also shows systematically higher temperatures than observed at altitudes >95 km, though the difference is much smaller than in EMAC. WACCM and HAMMONIA show no systematic differences compared to the observations, thus NO differences between these two models cannot be explained by temperature.

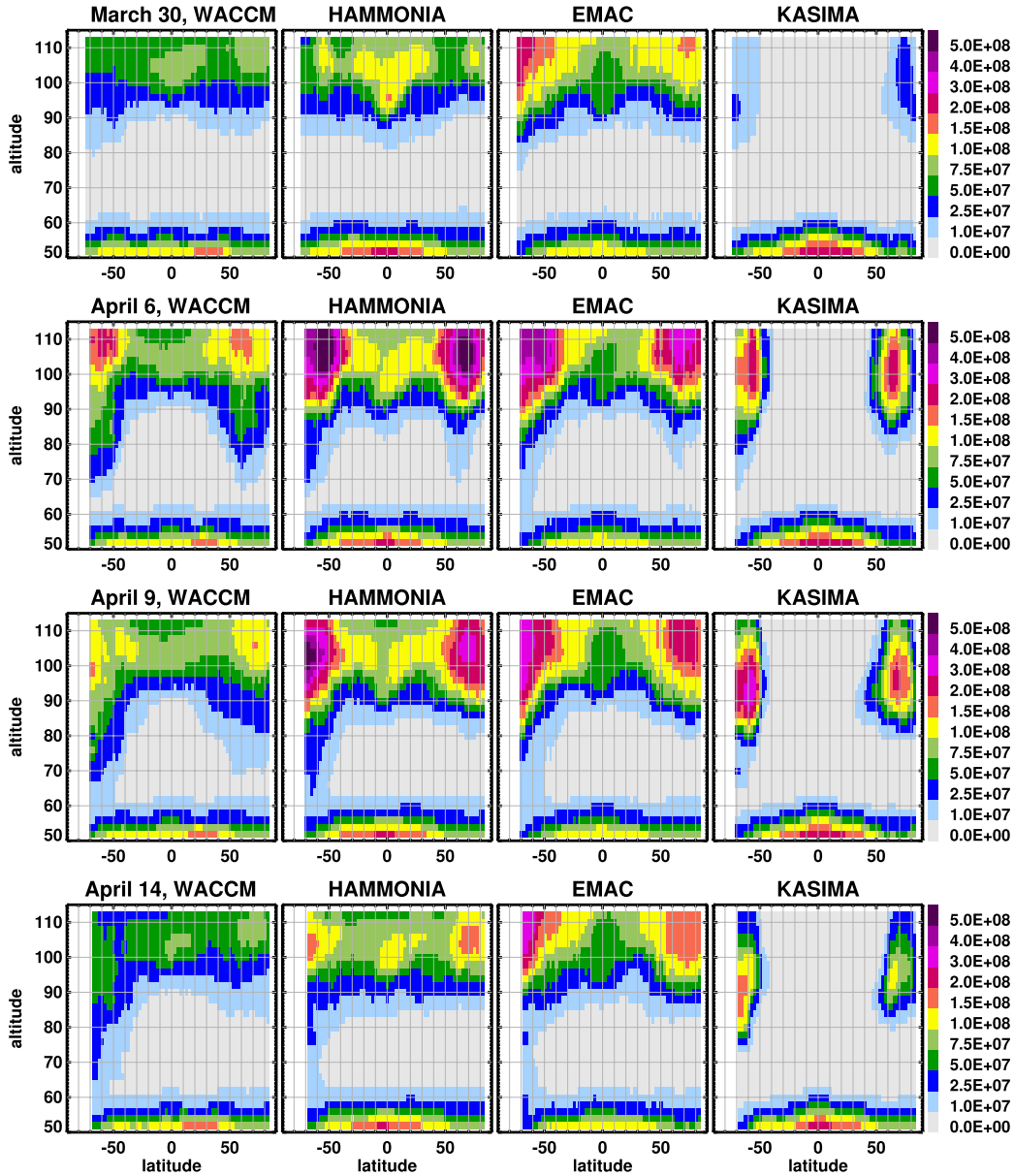

Figure 3. Daily mean zonal mean NO densities (cm^{-3}) for the core model experiments AIMOS on four days. From top to bottom: March 30 before the storm, April 6 during the storm main phase, April 9 in the recovery phase, April 14 at the end of the period of geomagnetic activity. Model results on SCIAMACHY footprint in the illuminated atmosphere from 50–115 km altitude. From left to right: WACCM, HAMMONIA, EMAC, and KASIMA.

2.2.7. Model Sensitivity Studies: Mechanism of NO Formation, Transport and Mixing

To further investigate the reasons for the large discrepancies in the NO amounts of the four chemistry climate models while using the same set of electron ionization rates, the relative contributions of different sources of NO to the overall NO budget are investigated in the following, based on the sensitivity model experiments Sens1 to Sens6.

The relative contributions of the different NO formation mechanisms to the overall NO budget are estimated by comparing the NO amount in the respective sensitivity model experiment to the NO amount in the AIMOS core experiment of the same model, which considers all NO formation mechanisms as outlined in Table 3. Note, however, that this is only an approximation of the relative contributions, as due to the internal dynamical variability of the models, differences in transport and mixing between model experiments of the same model might lead

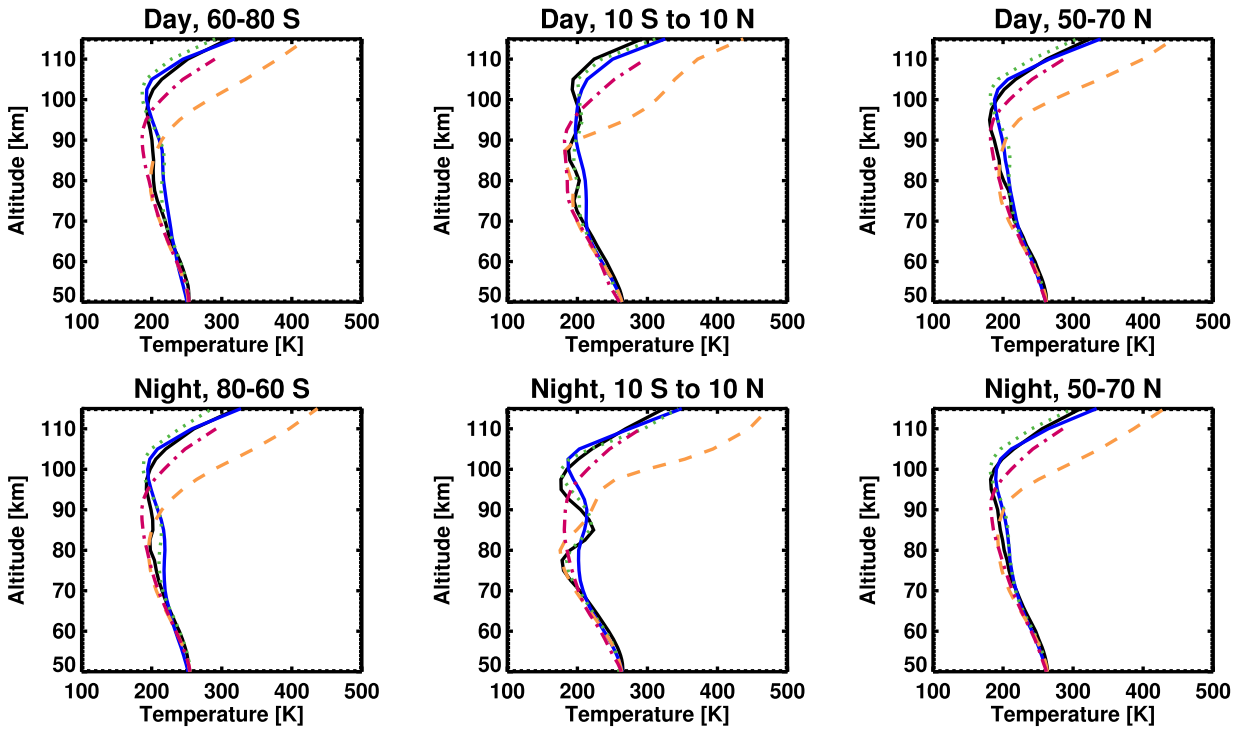

Figure 4. Comparison of zonal mean temperatures from the MIPAS upper atmosphere mode (black solid line) on 30 March 2010, for daytime (above) and nighttime (below), to model results on the respective satellite footprint (WACCM blue dashed-dot-dot, HAMMONIA green dotted, EMAC orange dashed and KASIMA red dash-dot), in three latitude regions: high Southern latitudes (left), tropics (middle), moderately high Northern latitudes (right).

to additional differences in the NO amounts, particularly at the edge of the areas with large NO amounts where gradients are large.

In Figure 5, the relative contribution of electron precipitation (auroral and MEE, III) is shown for all four models for March 30, April 6, April 9 and April 14. During the quiescent period before the storm (March 30), the contribution of electron impact ionization to the overall NO amount is less than 20% in HAMMONIA, (10–30)% in EMAC and WACCM at high latitudes above 70 km, and 30%–90% in the high-latitude upper mesosphere and lower thermosphere above 70 km in KASIMA. Negative and large positive values exceeding 50% appear in small hotspot areas above 70 km in WACCM, HAMMONIA and EMAC, but not in KASIMA, presumably triggered by small changes to the model dynamics due to their internal dynamical variability. During the geomagnetic storm on April 6, the contribution of electron ionization to high-latitude NO exceeds 50% above 65 km(SH)/70 km(NH)

Table 3
Calculation of the Contributions of I Auroral Electrons, II MEE, III all Electron Precipitation, IV Photoionization, V Upper Boundary Condition and VI Proton Ionization From the Sensitivity Model Experiments Compared to the Core Model Experiment

Contribution by	Model experiments	Contributing models
I: Auroral electrons	$\frac{AIMOS-Sens1}{AIMOS}$	all
II: MEE	$\frac{AIMOS-Sens2}{AIMOS}$	all
III: Aurora + MEE	$\frac{(AIMOS-Sens1)+(AIMOS-Sens2)}{AIMOS}$	all
IV: Photoionization	$\frac{Sens1-Sens3}{AIMOS}$	HAMMONIA, EMAC, KASIMA
V: NO upper boundary	$\frac{Sens1-Sens5}{AIMOS}$	WACCM
VIa: Proton ionization	$\frac{Sens3-Sens4}{AIMOS}$	HAMMONIA, EMAC, KASIMA
VIb: Proton ionization	$\frac{Sens5-Sens6}{AIMOS}$	WACCM

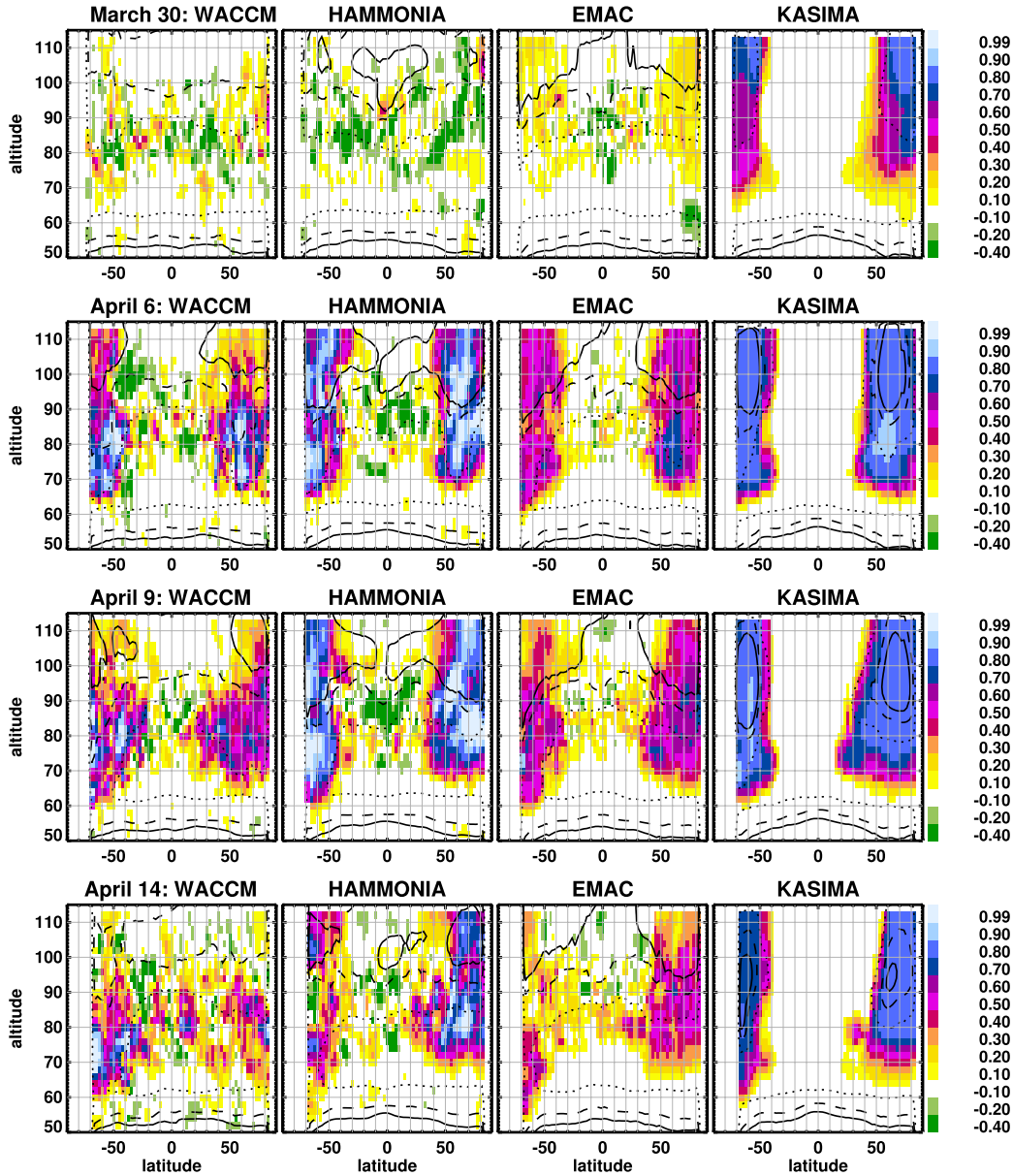

Figure 5. Relative contribution of electron precipitation (auroral and MEE) to the overall NO amount. From left to right: WACCM, HAMMONIA, EMAC, and KASIMA. From top to bottom: March 30, April 6, April 9, April 14.

in all models. The relative contribution is lowest in EMAC (less than 80%), highest in HAMMONIA and WACCM (more than 90%). In WACCM, the relative contribution decreases to (10–60)% above 100 km. After the event, on April 9 and 14, the relative contribution of electron ionization to the overall NO amount decreases slightly, but stays above 50% in all models in clearly defined areas. However, the locations of these areas strongly affected by electron ionization change over time, indicating the influence of transport and mixing processes. In the Northern hemisphere, the lowermost edge of these areas mostly stays above 70 km altitude in all models, while the area shifts equatorwards in the upper mesosphere, extending to 30°N in HAMMONIA and EMAC, to about 10°N in WACCM and KASIMA. In the Southern hemisphere, the area with relative contributions of electron ionization of more than 50% progresses downward with time, reaching 60 km on April 9 in all models, and extending below 60 km on April 14 in EMAC. In WACCM, the area also extends equatorwards to 20°S in the Southern hemisphere upper mesosphere (70–90 km), presumably indicating strong meridional transport and mixing in WACCM not observed in the other models here.

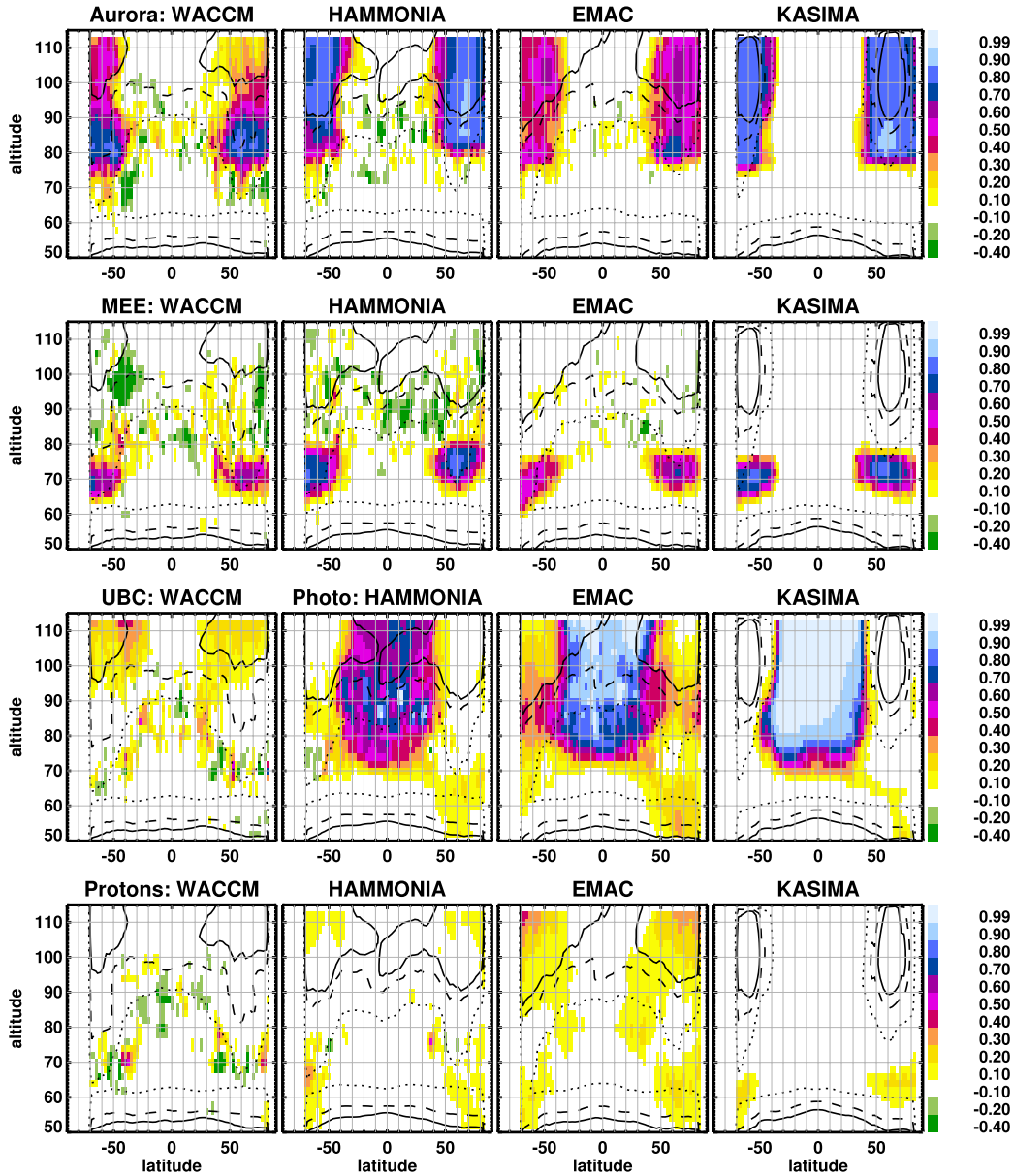

Figure 6. Relative contribution of different NO formation mechanisms to the overall NO amount for the storm main phase on 6 April 2010. From top to bottom: auroral electrons; medium-energy electrons; photoionization (HAMMONIA, EMAC, KASIMA) respectively upper boundary condition (WACCM); solar protons (WACCM) respectively solar and soft protons (HAMMONIA, EMAC, KASIMA). From left to right: WACCM, HAMMONIA, EMAC, and KASIMA.

In Figure 6, the relative contributions of auroral electrons (I), medium-energy electrons (II), the upper boundary conditions (WACCM, V) respectively photoionization (HAMMONIA, EMAC, KASIMA, IV) and proton ionization (VIa and VIb) are shown. Despite the clear cut between auroral and MEE ionization in the setup of the model experiments Sens1 and Sens2, areas of significant contributions overlap, indicating cross-mesopause transport or mixing during the event. This is most pronounced in WACCM. Photoionization dominates NO formation in mid- and low latitudes above 75 km in KASIMA (80%–100%), EMAC (70%–100%) and HAMMONIA (40%–90%). The situation is likely similar in WACCM, but model experiments without photoionization were not carried out with this model. The lower relative contribution of photoionization in HAMMONIA compared to EMAC and KASIMA could be due to a thermal feedback acting in HAMMONIA but not in KASIMA and EMAC, as only in HAMMONIA NO from the model experiment itself is used for the calculation of NO radiative cooling rates in experiment Sens3. In KASIMA, a constant NO profile is used in all model experiments for the radiative cooling

rates, and in EMAC, NO from the AIMOS model experiment is used in experiment Sens3. In HAMMONIA and EMAC, a small contribution of about (10–30)% of photoionization is also shown for the high-latitude Northern hemisphere mesosphere down to at least 50 km, presumably due to downward propagation of thermospheric NO during the preceding winter months. This small contribution is also observed in KASIMA but confined to the equatorward edge of the polar area, possibly indicating poleward and downward transport from the low-latitude uppermost mesosphere. In WACCM, the upper boundary condition contributes (10–40)% to the overall NO budget above 95 km at high and mid-latitudes in both hemispheres, which is likely the reason that the relative impact of electron ionization is smaller there than in the upper mesosphere below 90 km. Proton ionization contributes to the overall NO amount in high latitudes in both hemispheres in the thermosphere above 90 km in EMAC and HAMMONIA, indicating a contribution of soft protons to the high-latitude auroral NO during the event for the two models with top altitudes well above 120 km. A contribution of proton ionization of (10–30)% to the overall NO budget is also shown at high latitudes in both hemispheres in HAMMONIA, EMAC, and KASIMA. This could be interpreted as a contribution of higher-energy solar protons to the mesospheric NO enhancement during the geomagnetic storm, however, the same structure is not observed in WACCM. In WACCM, no indication of an impact of solar protons on the overall NO budget is shown during this day with the exception of one hotspot in 40–50°S and 70–80 km altitude where the relative contribution exceeds 50%. As this lies at the edge of the Southern hemisphere mesospheric NO enhancement, it could likely be due to internal dynamical variability of the model affecting equatorwards transport of the polar NO in this model.

2.2.8. Summary: Chemistry-Climate Models

A comparison of all chemistry-climate models has revealed significant differences of up to an order of magnitude in nitric oxide, despite using the same electron ionization rates in the specified dynamics mode. A number of reasons for these differences have been analyzed:

- too-high temperatures in the lower thermosphere driving thermal NO formation in EMAC
- the different parameterizations of photoionization used by WACCM, HAMMONIA and EMAC on the one hand, by KASIMA on the other hand
- differences in transport and mixing, with stronger cross-mesopause transport as well as stronger equatorwards transport contributing to a stronger mesospheric NO signal extending further down into the mesosphere as well as further into midlatitudes in WACCM
- possibly even the model top height, limiting the amount of high-latitude NO in the models with lower top height (WACCM and KASIMA) due to a lack of soft electron and proton precipitation. This is compensated for by an upper boundary condition, and high-latitude NO for example, in WACCM significantly depends on the upper boundary condition above 100 km

2.3. Satellite Observations of Nitric Oxide

We use observations of nitric oxide (NO) in the mesosphere and lower thermosphere from three satellite instruments: SOFIE on AIM (see Section 2.3.1), SCIAMACHY on ENVISAT (Section 2.3.2) and MIPAS on ENVISAT (Section 2.3.3). SCIAMACHY and MIPAS provide near-global coverage within one day, while SOFIE measures in solar occultation geometry and provides data from a restricted latitude area corresponding to the terminator crossings (Sunrise and Sunset) of each orbit. The orbit of ENVISAT has an equator crossing time of 10 am/pm, while the orbit of the AIM satellite crosses the equator at noon and midnight. All three instruments observe several hours after the local maximum in auroral (several keV) electron precipitation around magnetic midnight in the Southern hemisphere, with SOFIE observing before, MIPAS and SCIAMACHY observe within the local maximum of medium-energy (100–300 keV) electrons around 10–12 magnetic local time, see Yakovchuk and Wissing (2019).

The SCIAMACHY NO observations are derived from resonant scattering and are thus only available during daytime, covering the illuminated part of the globe. MIPAS observations are derived from thermal emission and are independent of solar illumination. SCIAMACHY and SOFIE observations are available as daily data, while MIPAS observations in the Upper Atmosphere (UA) and Middle Atmosphere (MA) modes, which extends into the lower thermosphere, are available every five days. From MIPAS, data observed in the nominal (NOM) mode are available daily, but those are limited to below 70 km. We use MIPAS MA/UA data of 5 days, March 25 and March 30 (quiet time before the increase in geomagnetic activity starting April 1), April 4 (enhanced activity

Table 4
Overview of Satellite Instruments Providing NO Data Sets

Instrument	SOFIE	SCIAMACHY	MIPAS
Satellite	AIM	ENVISAT	ENVISAT
Equator crossing time	noon/midnight	10 am/pm	10 am/pm
Coverage	70–80°S	near-global	Global
Altitudes [km]	35–115 km	64–90 km	40–115 km (UA) 10–70 km (NOM)
Illumination	Sunset	Daytime	day and night
Temporal coverage	Daily	Daily	every 10 days (UA) daily (NOM)

Note. Note that coverage and illumination apply to the data used here as available during mid-March to end of April 2010.

before the storm onset), April 9 (recovery phase after the geomagnetic storm on April 5-6), April 14 (after the storm) as well as daily MIPAS NOM data in 60–70 km altitude at high Southern latitudes for days without MA/UA observations. A comparison of important features of the three satellite instruments during the period mid-March to end of April 2010 is provided in Table 4. A comparison of NO densities observed by the three satellite instruments during this time is provided in Section 2.3.4.

2.3.1. SOFIE/AIM

The Solar Occultation for Ice Experiment *SOFIE* onboard the AIM satellite has been in a sun-synchronous orbit with Equator crossing time of noon/midnight since early 2007 (Gordley et al., 2009). SOFIE measures absorbed solar light in solar occultation geometry, from the UV to the IR wavelength range in 16 bands between 0.29 and 5.3 μm. Local sunrise and local sunset data are obtained during each orbit, providing 15 geolocations per day, in each hemisphere in a narrow latitudinal band within 65°–85° depending on time of year. During 2010, relative to the satellite, sunrise was in the Northern, and sunset in the Southern hemisphere, see, for example, sofie.gats-inc.com/. However, after the March equinox, it was polar night in the Southern hemisphere and sunset relative to the satellite referred to local sunrise; vice versa for the Northern hemisphere. The SOFIE NO data are derived from the 5.3 μm transitions, and in this study, we use the NO data version 1.3, from mid-March to end of April 2010. The SOFIE data are provided between 35 and 150 km on a 200 m altitude grid, but with an intrinsic altitude resolution of about 2 km. To reduce noise in the data, a 2 km running average is applied in the vertical. The SOFIE NO data have been compared against MIPAS and ACE/FTS (Hervig et al., 2019), showing an agreement within 50% in the altitude range 60–105 km for sunrise, and in the range 60–140 km for sunset observations. Below 65 km altitude, SOFIE NO is systematically lower than both MIPAS and ACE, with differences on average larger than 50% below 60 km (Hervig et al., 2019). SOFIE data also exhibit large uncertainties below 80 km due to interference from H_2O absorption and thermal response, especially for the sunrise observations. Therefore we mostly use data from the sunset mode (Southern hemisphere) in the altitude range 60–115 km in the following. The latitudinal coverage of the data used varies from about −80° at the beginning to about −70° at the end of the time period.

SOFIE level 2 data products are available at sofie.gats-inc.com.

2.3.2. SCIAMACHY/ENVISAT

The SCanning Imaging Absorption spectroMeter for Atmospheric CHartographY *SCIAMACHY* was one of three atmospheric sounding instruments on board the European ENVironmental SATellite *ENVISAT* which was orbiting in a sun-synchronous orbit at around 800 km altitude with Equator crossing times at 10:00 and 22:00 local time, from August 2002 until communication to the satellite failed in April 2012. It measured in the UV–vis–NIR spectral range from about 230 to 2,300 nm, consecutively in limb, nadir, solar, and lunar occultation measurement geometry; for a detailed instrument description, see Burrows et al. (1995) and Bovensmann et al. (1999). NO number densities were retrieved from the SCIAMACHY nominal limb mode (NOM, daily scanning the atmosphere within ≈ 0–93 km) using the NO γ-band emissions around 250 nm (Bender et al., 2013, 2017a, 2017b). Since those emissions are fluorescent emissions excited by solar UV radiation, SCIAMACHY NO data are only available for the dayside part of the orbit. In this study, we use SCIAMACHY NO data from version 6.2.1 (Bender,

Sinnhuber, Langowski, & Burrows, 2017), which are derived by an orbitwise 2-D retrieval on a 2.5° × 2 km latitude×altitude grid for every orbit retrieved, with a vertical resolution of about 5–10 km and an along-track horizontal resolution of about 9°. SCIAMACHY NO data from the mesosphere-lower thermosphere limb mode (MLT, scanning the atmosphere in ≈53–151 km every 15 days) have been compared to MIPAS and other satellite data based on daily-mean zonal means, showing a generally good agreement between all instruments (Bender et al., 2015); a similar comparison for the data from the nominal limb mode used here is not yet available. When using the SCIAMACHY data here, the measurement sensitivities have been taken into account by evaluating the averaging kernel diagonal elements together with the solar zenith angle (SZA) at each retrieval grid point. In this analysis, only data with a diagonal element larger than 0.02 and a SZA lower than 86° have been considered, restricting the feasible altitude range to above 64–68 km in most cases. No binning or averaging of the retrieved densities has been applied.

SCIAMACHY level 2 NO data are available at https://www.imk-asf.kit.edu/2939.php and https://www.zenodo.org/record/1009078.

2.3.3. MIPAS/ENVISAT

The Michelson Inteferometer for Passive Atmosphere Sounding *MIPAS* (Fischer et al., 2008), also on board the ENVISAT satellite, measured the light emitted from the atmosphere in the IR wavelength range from 4.15 to 14.6 μm in limb scanning geometry. Both day and nighttime NO volume mixing ratio profiles used in this study were retrieved from spectrally resolved 5.3 μm emissions under consideration of non-local thermodynamic equilibrium as described in Bermejo-Pantaleón et al. (2011). Data from the Middle Atmosphere observation mode (MA, Version V8R_NO_561), the Upper Atmosphere observation mode (UA, Version V8R_NO_661) and from the nominal limb mode (NOM, version V8R_NO_261) were used. MA data are available on March 25, April 4, and April 14 with a vertical coverage of 18–100 km, UA data are available on March 30 and April 9 with a vertical coverage of 42–172 km, NOM data are available near-daily with a vertical coverage of 7–72 km. These data versions are updates of the previous versions V5R_NO_521, V5R_NO_622, and V5R_NO_220, respectively, and employ the most recent spectral radiance calibration ESA version 8.03, and improved a-priori parameter information. The vertical resolution of the MIPAS NO data is about 5–8 km below 70 km, about 8–12 km in polar regions above 70 km, and 12–20 km above 70 km outside polar regions. The along-track spacing of MIPAS footprints is about 515 km (430/410 km) in the UA (MA/nominal) mode, resulting in a latitude resolution of about 5° (4°). The NO volume mixing ratios are transferred into number densities using pressure and temperature information derived from MIPAS CO_2 15 μm emissions below 107 km and from NO 5.3 μm emissions above. Pressure is derived from the CO_2 emission below ≈50 km, from hydrostatic equilibrium above.

MIPAS level 2 NO data are available at https://www.imk-asf.kit.edu/english/308.php.

2.3.4. Intercomparison of NO Observations

A comparison of NO densities observed by the three satellite instruments is shown in Figure 7, exemplarily for 9 April 2010, in the recovery phase after the geomagnetic storm on the respective satellite footprints at 90 and 74 km altitude. A comparison of daily mean zonal mean densities of MIPAS and SCIAMACHY as a function of geomagnetic latitude in the altitude region covered by SCIAMACHY data (65–91 km) is shown in Figure 8 for March 30, April 9, and April 14, and a comparison between daily NO observations from MIPAS and SOFIE for the latitudinal and solar zenith angle range of the SOFIE observations is provided in Figure 9, for the period March 16 to April 25 in the altitude range 60–115 km.

A clear increase of NO during the geomagnetic storm compared to the quiet period before the onset of activity on April 1 is consistently observed in the high-latitude mesosphere (70–90 km) by all three instruments (Figures 7 and 8), in the lower thermosphere (90–115 km) by MIPAS and SOFIE (Figure 9). This NO increase is related to the auroral regions, as clearly shown in MIPAS and SCIAMACHY data (Figure 8), but with regions of enhanced NO extending into mid-and low latitudes over central Asia (30–60°N, 0–180°E), Indonesia (around the equator, 90–135°E) and west of Australia (15–45°S, 90–135°E) (Figure 7). MIPAS nighttime data show similar structures but higher absolute values than MIPAS daytime data. SCIAMACHY and MIPAS daytime NO generally agree well both in absolute values and in the morphology of areas of enhanced NO. However, there are also systematic differences: looking at individual observations, the spread between highest and lowest values in the auroral oval is larger in MIPAS than in SCIAMACHY data (Figure 7). In the zonal average, NO amounts in MIPAS and SCIAMACHY data are more consistent (Figure 8), though at high Southern latitudes polewards of

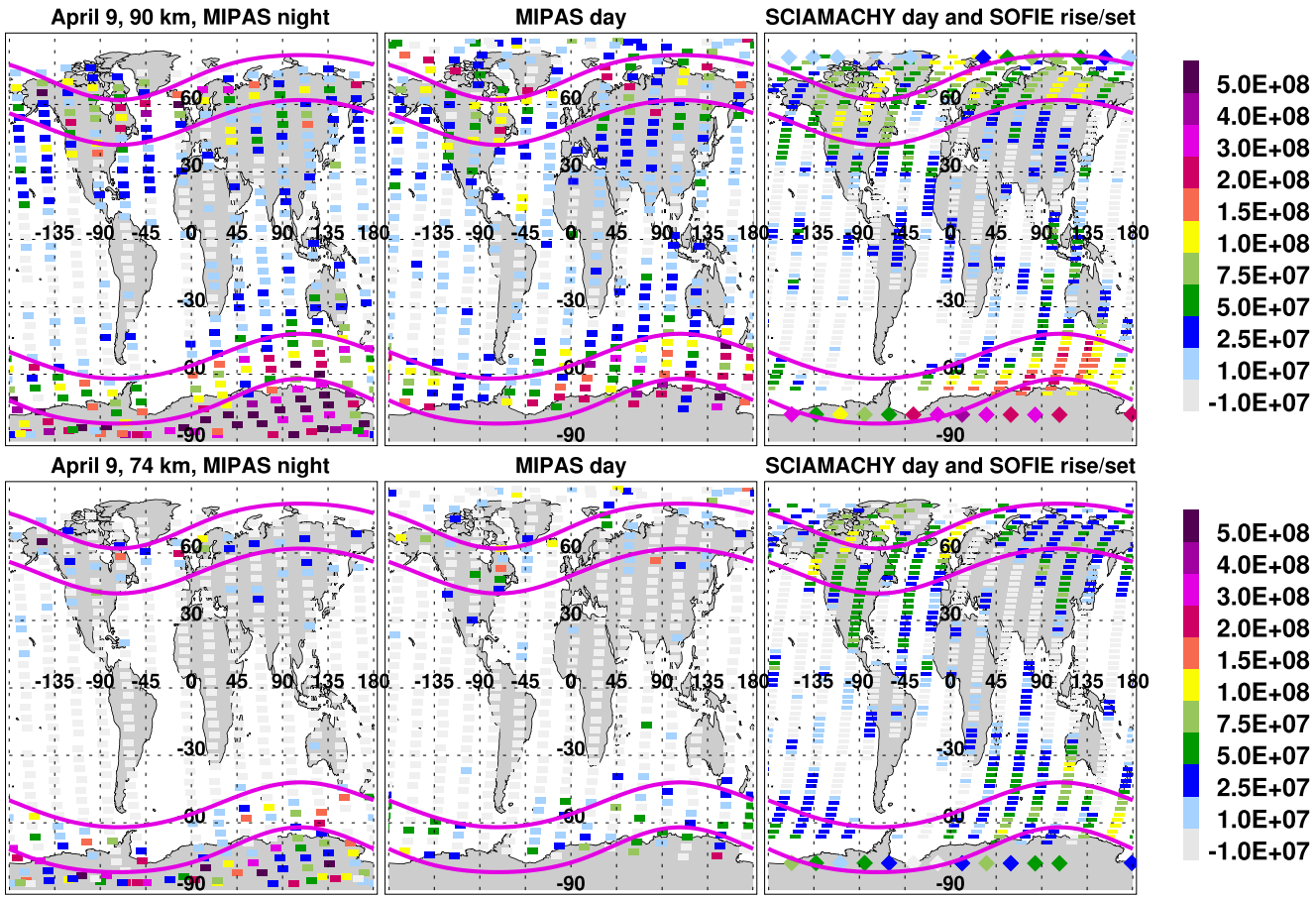

Figure 7. Comparison of NO densities (cm^{-3}) from MIPAS night (sza ≥ 94°, left) and daytime (sza ≤ 86°, middle) observations with SCIAMACHY (sza ≤ 86°, rectangles) and SOFIE (sza≈ 90°, rhombi) measurements (right) on 9 April 2010 in 90 and 74 km. Purple lines denote the approximate area of the aurorae and radiation belts (geomagnetic latitudes of 52° and 72°). The range ($-1\ 10^7$ to $1\ 10^7$) cm^{-3} of the lowest (light gray) contour interval represents the approximate noise floor of SCIAMACHY NO. *Note*. different footprints at high latitudes as SCIAMACHY observed in flight direction, while MIPAS observed backwards and adapted its viewing angle at high latitudes to point directly poleward.

70° on April 9 and 14, MIPAS daytime data show higher values than SCIAMACHY data; conversely, areas of enhanced NO extend further equatorwards in both hemispheres in SCIAMACHY data compared to MIPAS data in the mid-mesosphere around 70 km on April 9. These differences can likely be explained by the broad vertical resolutions and different vertical sensitivities of both instruments, as well as the broader along-track resolution of SCIAMACHY. Sunset observations of NO at high Southern latitudes from SOFIE and co-located MIPAS observations (Figure 9) agree well above 80 km both in absolute values and in the temporal evolution during and after the event. In 75–80 km altitude, MIPAS data during and after the event are systematically higher than SOFIE data, but still within the error bounds of both instruments. In 60–70 km altitude, MIPAS and SOFIE data agree well with the exception of one day after the event, April 9, when MIPAS observes significantly higher values than SOFIE, possibly due to differences in the sampling and overpass time during a period of large variability. Note MIPAS values on April 10 are even higher than on April 9, but there are no SOFIE data on this day. Higher MIPAS observations during the storm time could be due to the timing of the MIPAS overpass within the local maximum of MEE precipitation around 10–12 magnetic local time. In the pre-storm phase, SOFIE observations are significantly higher than MIPAS observations in 65–75 km. Finally, SCIAMACHY daytime NO and SOFIE sunset NO data at 74 and 90 km at high Southern latitudes on April 9 appear to be consistent both in absolute values and in the longitudinal structure of enhanced values, though there are no co-located observations due to the dependence of the SCIAMACHY NO observation on direct sunlight (Figure 7).

To summarize, all instruments agree that there was a substantial increase in NO throughout the high-latitude mesosphere during the geomagnetically active period in early April 2010, though systematic differences between

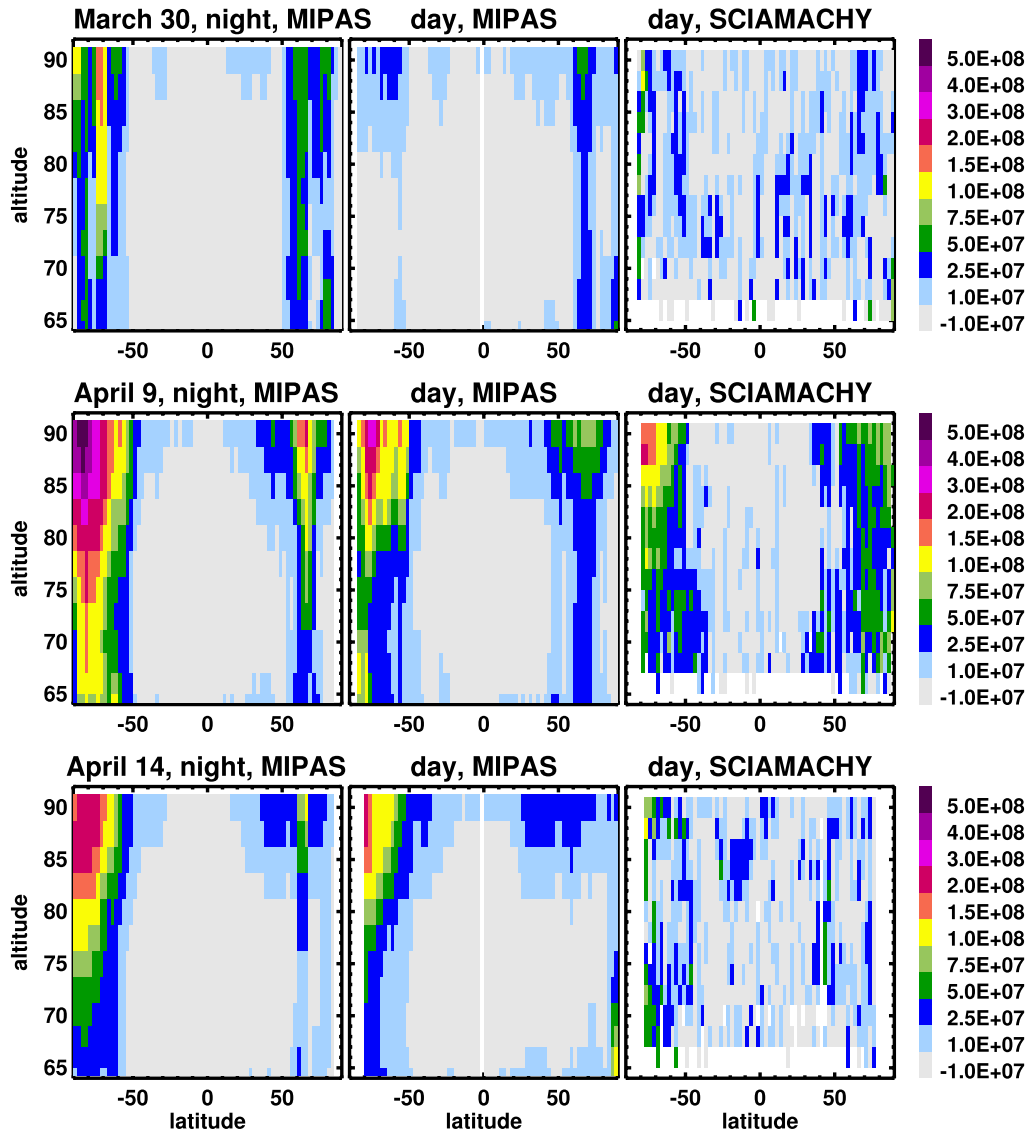

Figure 8. Comparison of NO densities (cm^{-3}) from MIPAS night (left) and daytime (middle) observations with SCIAMACHY (right) daily mean profiles as a function of geomagnetic latitude and altitude in the range where SCIAMACHY measurements are provided (66–92 km) for March 30 (upper panels), April 9 (middle panels) and April 14 (lower panels). To account for the spread of geomagnetic latitudes over geographic latitudes, data are averaged area-conserving considering the cosine of the latitudes.

MIPAS and SOFIE in the lowermost mesosphere, MIPAS and SCIAMACHY in the mid-mesosphere have to be taken into account when interpreting model-measurement intercomparisons as in Section 3.

3. Model-Measurement Intercomparison and Difference Between Ionization Rate Data-Sets

In the following, NO densities from the core model experiments AIMOS, APEEP, and OULU are compared against the satellite observations to assess the impact of the different ionization rate data-sets. The model results are interpolated spatially and temporally onto the footprints of the respective satellite observations, and multi-model mean (MMM) daily mean data are calculated for each core model experiment. Multi-model means are used here to emphasize differences due to the different ionization rate data-sets despite the large spread between the chemistry-climate models, to reduce the variance at the model site, and to provide a more robust model comparison. This is well justified in the mesosphere because there the differences between model results are mainly

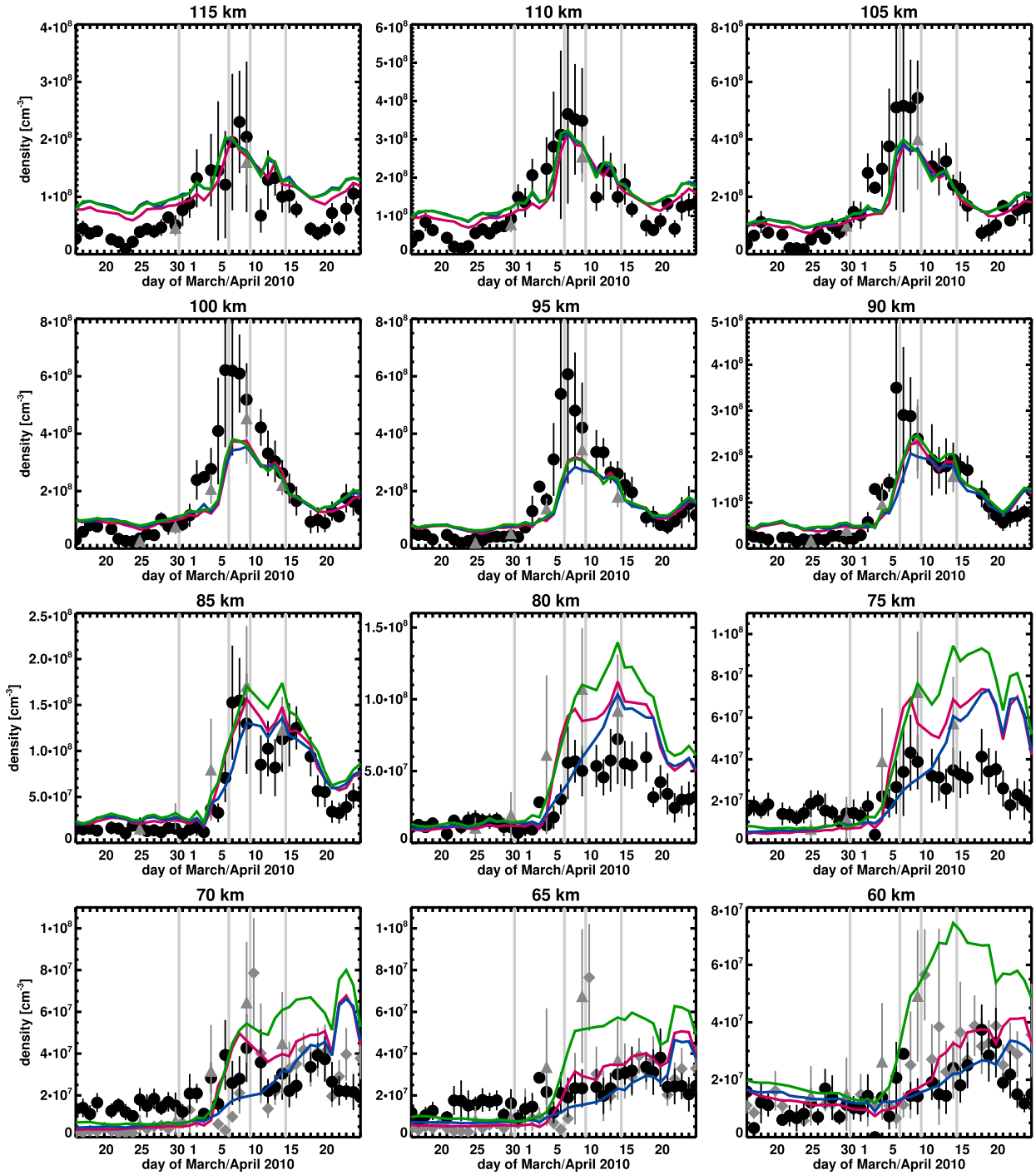

Figure 9. Comparison of daily mean multi-model mean (MMM) NO density results of the three core model experiments AIMOS (red), APEEP (blue), and OULU (green) from March 16 to April 24 on 5 km steps between 60–115 km on SOFIE footprints at high Southern latitudes. SOFIE (black circles), MIPAS MA/UA (gray triangles) and MIPAS NOM (gray rhombi) daily mean data are shown as reference. MIPAS data are averaged over the solar zenith angles and latitude area of the SOFIE data (80°–98° sza, roughly corresponding to sunset at 60 km and to ±3° around the mean latitude of SOFIE). Error bars are 2 times the standard error of the mean of the daily averaged observations. Note the different scale of NO densities in different altitudes. Marked as gray vertical lines are March 30, April 6, April 9, and April 14.

due to the dynamical state of the models; in the thermosphere, where systematic differences arise also due to the differences in the NO formation mechanism, the multi-model mean might diminish, but probably not erase, the impact of these systematic effects (see Section 2.2.7). The temporal evolution of NO at high Southern latitudes is investigated in Section 3.1, the latitudinal distribution of NO is investigated for four selected days in Section 3.2.

3.1. Temporal Evolution at High Southern Latitudes: SOFIE and MIPAS

The temporal evolution of NO at high Southern latitudes from March 16 to April 25 in the altitude range 60–115 km is shown in Figure 9. Daily observations from SOFIE, observations from two days from the MIPAS MA and UA modes each, and daily observations from the MIPAS NOM measurement mode below 70 km are compared to MMM results of the AIMOS, APEEP, and OULU model experiments, in the following referred to as AIMOS, APEEP, and OULU.

The observed NO in the lower thermosphere (95–115 km) increases steadily during the period of enhanced geomagnetic activity starting March 30 until the storm main phase on April 6, it continues to stay at high values until April 9, and then slowly decreases until reaching background values again around April 18. This temporal evolution manifests in a broad, nearly symmetric NO peak around the storm main phase. In the mesopause region (85–90 km), a moderate increase in NO is observed in early April (April 3–5, a sharp increase during the storm main phase on April 6 followed by a sharp decrease and a secondary increase on April 14–16 possibly indicating downward mixing from the lower thermosphere with a temporal delay of a few days, and decay from then until April 20. In the middle mesosphere (75–80 km), the onset of the NO increase is similar, but after that onset, constant values continue until April 18 (80 km) or 20 (75 km, possibly due to persistent down-mixing of enhanced NO across the mesopause. During this period, MIPAS data are higher than SOFIE data but show the same general behavior. At 70 km, NO increases from April 4 to the recovery phase on April 10. At 65 km, a short, small increase in NO is observed on April 3-4. After this period, a steady increase is observed until April 20. Another sharp increase on April 9-10 is only observed by MIPAS, possibly indicating large variability on this day. At 60 km, the behavior is similar to 65 km, though the increase on April 4 is observed only by MIPAS, and similar, small increases are observed during the event on April 6-7 (SOFIE) respectively April 8 (MIPAS). The secondary increase around April 14 in 85–90 km, the nearly constant values in 75–80 km from the storm main phase until around April 18/20, and the increase from the storm onset to around April 20 below 75 km suggest mixing of the lower thermospheric NO signal into the upper mesosphere, and downward transport and mixing throughout the mesosphere after the geomagnetic storm. In 85–90 km, the sharp increase during the storm main phase indicates a mixture of local production and downward transport. Below this altitude, there is no clear indication for direct production during the event on the SOFIE footprint: an increase on April 5/6 is observed in SOFIE data in 80 and 60 km, but in MIPAS observations there as well as in SOFIE observations in 65–75 km, NO enhancements already start before the event.

The MMM results from all three core model experiments are nearly identical in the lower thermosphere and mesopause region (90–115 km). This is expected as AIMOS electron ionization rates are used in all model experiments except in WACCM core experiments APEEP and OULU, where the internally generated aurora of WACCM is used. The small difference at 105–115 km between AIMOS on the one hand, and APEEP and OULU on the other hand presumably reflects this difference in auroral forcing. At 105–115 km, the MMMs overestimate NO compared to the observations during the geomagnetically quiet periods, but they agree well during the storm phase. At 90–100 km, the MMMs still slightly overestimate NO during the geomagnetically quiet periods, but during the geomagnetically disturbed period, MMM results are low, at or below the lower error bound of the observations. The slow decline of NO after the storm main phase is well captured by the MMMs at and above 85 km. Around 85 km, differences between the MMMs based on different ionization rate data-sets become more pronounced during and particularly after the storm main phase. In 70–85 km altitude, AIMOS and OULU agree well during the storm onset and main phase (April 5-8) but are higher than APEEP. After the storm main phase from April 9 to at least April 20, OULU is higher than AIMOS and APEEP, while AIMOS converges to APEEP; after April 17, AIMOS and APEEP are nearly identical again. At 85 km, AIMOS and APEEP agree reasonably well with the observed NO during and after the geomagnetic storm, while OULU overestimates NO during April 9–14. At 75–80 km, the increase in NO during the event (April 6–8) is overestimated by OULU and AIMOS, but it is well represented by APEEP. After April 9, NO is overestimated in the MMMs of all core experiments with the exception of April 9, when they are within the error bounds of the MIPAS observation, and April 14, when AIMOS and APEEP are within the error bounds of the MIPAS observation. This again highlights the high variability of NO as observed by MIPAS during this time, and presumably argues that the MMM results are on average too high during this time, but still within the observed variability. At 70 km, MMM results of all three core experiments are in the range of the observed spread until April 9, when OULU and AIMOS agree well with observations, but APEEP is significantly lower. On April 10, only MIPAS data are available, and the MMMs of all core

model experiments are significantly lower than the MIPAS data. After April 10, AIMOS and APEEP agree well with observations, while OULU is significantly higher with the exception of April 11 and 14, when it is within the error range of the MIPAS observations. In 60–65 km, OULU shows highest, APEEP lowest NO densities, with AIMOS intermediate, during and after the storm onset. At 65 km, the AIMOS and APEEP agree well with observations until April 20 with the exception of April 3-4 and April 10, when they are significantly lower than the available observations, and April 9, when they are lower than MIPAS observations but in good agreement with SOFIE observations. Conversely, OULU NO densities are significantly higher than observations after April 6 with the exception of April 9 and 10 when they are within the error range of the MIPAS observations. On April 3-4, OULU NO densities are also lower than observations. After April 20, all MMMs are significantly higher than the observations. At 60 km, OULU NO densities are in good agreement with SOFIE observations but higher than MIPAS observations, during April 6-7, in good agreement with MIPAS observations but higher than SOFIE observations on April 9-10. Conversely, AIMOS and APEEP are in good agreement with MIPAS observations during April 6-7, in good agreement with SOFIE observations on April 8-11, but significantly lower than MIPAS observations on April 9-10. After April 11, APEEP agrees well with SOFIE observations, AIMOS agrees well with MIPAS observations which show slightly higher values on some days, OULU is significantly larger than observations. After April 22, MMMs of all three core model experiments are significantly higher than observations. MMMs of all three core model experiments clearly show vertical mixing from the lower thermospheric NO signal into the upper mesosphere and vertical transport and mixing throughout the mesosphere after the geomagnetic storm, qualitatively in agreement with the observations. However, the higher NO densities after the geomagnetic storm in 75–80 km in the MMMs of all three model experiments suggest too strong vertical transport/mixing in the upper mesosphere at least at these high Southern latitudes, while the distinctly higher densities in the OULU MMMs in 60–75 km are presumably due to a combination of higher local production and downward transport.

3.2. Latitudinal Distribution on Selected Days: SCIAMACHY and MIPAS

In Figure 10, the latitudinal distribution of daily mean NO in the mesosphere is shown on four days (March 30, April 6, April 9, April 14) for SCIAMACHY compared to AIMOS, APEEP, and OULU on the footprints of SCIAMACHY observations. The vertical range is restricted to 64–92 km by the availability of SCIAMACHY NO data. During the quiet time before the storm (March 30), the SCIAMACHY NO densities are at or below the detection limit throughout the whole altitude range and at all latitudes shown, with values at or below 2.5×10^7 cm^{-3}, and with no discernible coherent structures. MMMs of all three core model experiments show consistent features of moderately enhanced NO above 85 km, with highest values of more than 2.5×10^7 cm^{-3} at high Southern latitudes, values in the range (1–2.5)$\times 10^7$ cm^{-3} above 87 km at all latitudes, above 81 km (AIMOS) respectively 79 km (APEEP, OULU) at high Southern latitudes, and values below the noise floor of SCIAMACHY ($\leq 10^7$ cm^{-3}) everywhere else. Considering the high noise level of the SCIAMACHY observations, the model results are on average in reasonable agreement with the observations on this day. During the storm main phase (April 6), enhanced values of (5–10)$\times 10^7$ cm^{-3} are observed by SCIAMACHY throughout the whole altitude range at high latitudes polewards of 50° in both hemispheres, extending to mid-latitudes (≈40°) in the middle mesosphere (70–76 km). The SCIAMACHY NO densities reach more than 1×10^8 cm^{-3} in a narrow latitude area (60–70°N/S) above 86 km. It is not possible to distinguish from the SCIAMACHY observations of April 6 alone whether these clearly enhanced mesospheric NO values are due mainly to local production in the mesosphere, or due to downward transport and mixing from the lower thermosphere between March 30 and April 6; this is discussed in more detail in Section 3.3. MMM results of all three core experiments are very similar to each other at low and mid-latitudes, and agree well with observations there. At high latitudes, all three core model experiments show enhanced NO densities compared to the pre-storm period, down to at least 75 km (APEEP, Northern hemisphere), 70 km (AIMOS, Northern hemisphere), respectively over the whole altitude range to at least 65 km (OULU, Northern hemisphere; all core model experiments, Southern hemisphere). Absolute values of the MMMs vary, with the highest values generally shown in OULU, lowest values in APEEP, and AIMOS values intermediate between those. These differences in absolute NO amounts during the geomagnetic storm, and their spatial coverage, are consistent with results shown in Section 3.1 for the same altitude region, and with differences in the ionization rate data for this day (see Figure 2). Above 86 km altitude, the MMMs of all three core model experiments agree qualitatively well with the observations, although the magnitude of the NO values in the Northern hemisphere is slightly lower than observed in all MMMs, higher than observed in the Southern hemisphere in OULU. At high latitudes below 86 km, AIMOS and APEEP underestimate the enhanced NO

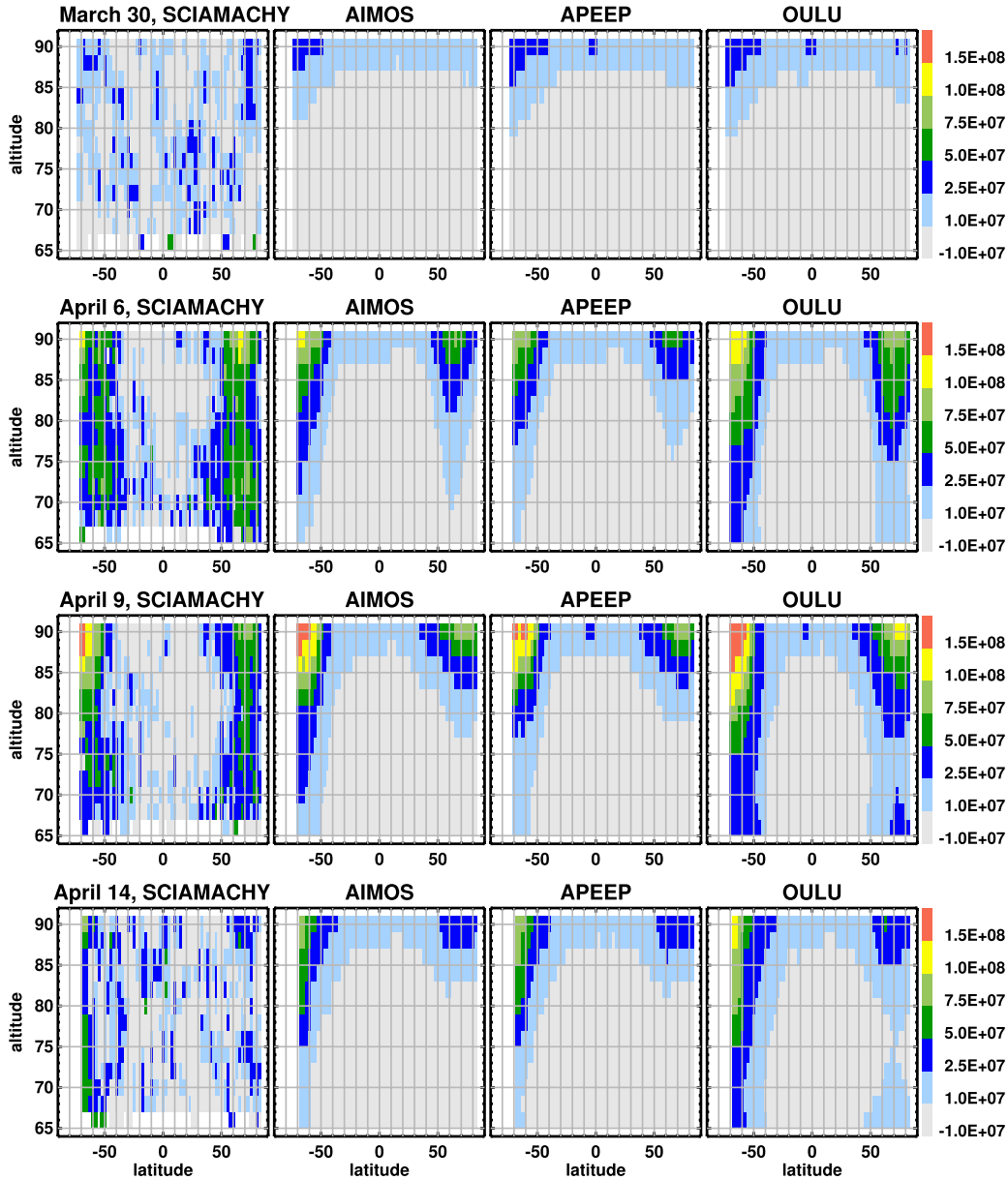

Figure 10. Left panels: SCIAMACHY daily mean NO density (cm^{-3}) on four days: March 30 before the storm (top), April 6 during the storm main phase (upper middle), April 9 in the recovery phase (lower middle) and April 14 after the storm phase (bottom). Middle to right panels: multi-model mean results of AIMOS, APEEP, and OULU core model experiments. The range of the lowest contour interval ($(-1 - 1) \times 10^7$ cm^{-3}) corresponds to the approximate noise floor of SCIAMACHY NO.

compared to the SCIAMACHY observations, both in magnitude and in the horizontal extent of the enhancement; OULU agrees well with SCIAMACHY observations in the Northern hemisphere in 80–86 km but shows higher values than SCIAMACHY in this altitude region in the Southern hemisphere. Below 80 km, OULU also underestimates NO densities compared to SCIAMACHY data. During the recovery phase (April 9), the SCIAMACHY data show a continuing increase of NO at high Southern latitudes above 80 km which is indicative of downward transport or mixing from the lower thermosphere, but a decrease compared to the storm main phase everywhere else. This behavior is generally well reproduced by the MMMs of all model experiments, although the magnitude of the enhancement is still underestimated below 80 km (AIMOS, APEEP) respectively 75 km (OULU) in the Southern hemisphere, and below 86 km (AIMOS, APEEP) respectively 84 km (OULU) in the Northern hemisphere. A secondary enhancement evolves below 70 km in the Northern hemisphere in OULU, in reasonable agreement with the SCIAMACHY observations at high Northern latitudes. This enhancement is

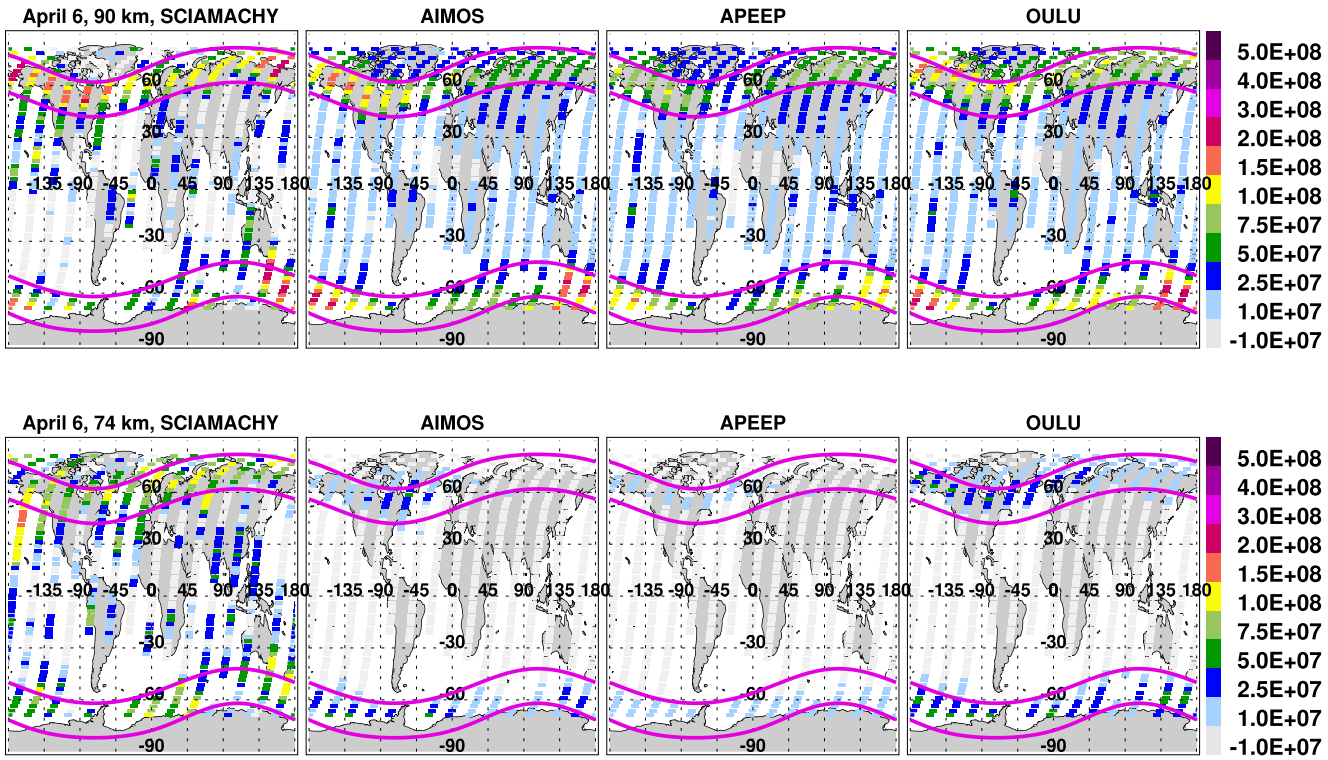

Figure 11. Left panels: SCIAMACHY NO density (cm^{-3}) during the storm main phase (April 6) in two altitudes: 90 km (top) and 74 km (bottom). Middle to right panels: multi-model mean daily mean results of model experiments using AIMOS, APEEP, and OULU ionization rate data-sets. Purple lines mark the position of the auroral ovals (52°/72°N/S geom.). The range of the lowest (light gray) contour interval (($-1 - 1$) $\times 10^7$ cm^{-3}) corresponds to the approximate noise floor of SCIAMACHY.

presumably due to the continuing ionization after the geomagnetic storm, which is present only in the OULU data-set (see Figure 2). After the storm (April 14), the SCIAMACHY observations indicate that the enhanced values of NO have decreased considerably everywhere with the exception of the high Southern latitude mid-mesosphere (65–79 km). There, enhanced values of more than 2.5×10^7 cm^{-3} persist, presumably due to downward transport from the uppermost mesosphere and lower thermosphere after the storm main phase. This behavior is reproduced qualitatively well in the MMMs of all three model experiments, though absolute values are lower than observed below 80 km (AIMOS, APEEP) respectively 75 km (OULU). The apparent downward transport of enhanced NO from the upper mesosphere to the lower mesosphere as observed by SCIAMACHY on April 9 and 14 at high Southern latitudes is consistent with SOFIE observations; however, the comparison of MMMs with SOFIE and MIPAS observations at high Southern latitudes polewards of the region covered by SCIAMACHY data shows significantly different results below 85 km, see Section 3.1.

To investigate the spatial coverage of enhanced NO during the event further, SCIAMACHY NO observations, as well as the MMMs of the core model experiments, are shown for individual SCIAMACHY footprint points at two altitudes (90 km, 74 km) for the storm main phase (April 6) in Figure 11. Note that there are no data-points when the satellite is within the South Atlantic Anomaly. In both altitude regions, enhanced values of NO are mostly confined to areas roughly within an extended auroral oval region defined by geomagnetic latitudes between 52° and 72°, in both the observations and the MMMs of all core experiments. At 90 km altitude, the MMMs of all three core model experiments are very similar to each other because three of the four chemistry-climate models use auroral electron ionization from the AIMOS data-set for all three core model experiments, and auroral electrons still dominate electron precipitation in 90 km. The MMM results agree very well with the observations within the auroral ovals, reproducing both the absolute values reaching up to 3×10^8 cm^{-3} in well-pronounced hotspot areas, as well as the locations of some of these hotspots over Northern America and South and South-East of Australia. However, the longitudinal extent of the Northern hemisphere hotspot is smaller in the MMMs than in the observations, with lower values over North-East Asia. The SCIAMACHY observations and the MMM results of all three model experiments show areas of enhanced NO extending from the auroral regions

into mid-latitudes. However, the locations of these areas are different; they are located over North America in the SCIAMACHY observations but over Asia in the MMM results of all three core model experiments. As they are located in the same place in all three core model experiments, these extensions into mid-latitudes are more likely due to horizontal transport than local production at geomagnetic mid-latitudes in the model results. Midlatitude NO enhancements have previously been observed after geomagnetic storms in the lower thermosphere around 110 km, see, for example, Richards (2004). These have been interpreted based on 1-dimensional and 3-dimensional model studies as a consequence of enhanced NO formation by Joule heating above 120 km and subsequent downward diffusion and horizontal transport (Dobbin & Aylward, 2008; Richards, 2004), and this mechanism could be responsible for the enhanced mid-latitude NO here, both in observations and in model results. At 74 km altitude, the results of all three core model experiments show enhanced values of NO in the auroral regions with very similar spatial features, but varying magnitudes; again, absolute values are highest for OULU, lowest for APEEP. Absolute values of all three core model experiments are lower than in the observations, and enhanced values are restricted strictly to the auroral oval regions in the model results, while the observations show additional regions of enhanced NO densities equatorwards of the auroral regions in the North-East Pacific (15–60°N, 135–180°W) and South/South-East of Australia (45–60°S, 135–180°E).

Daily mean zonal mean NO densities from the MIPAS UA observations and from the multi-model mean results of the core model experiments AIMOS, APEEP, and OULU on the MIPAS footprints are shown in Figure 12, separately for daytime and nighttime in the mesosphere and lower thermosphere (50–115 km) for two days, March 30 and April 9. In the low- and midlatitude thermosphere above 90 km, the MMMs of all three core model experiments overestimate NO compared to observations by a factor of 2–3 during daytime and 2–8 during nighttime on both days, possibly indicating an overestimation of the impact of photoionization in the three chemistry-climate models using the Solomon and Qian (2005) photoionization rates. In the high-latitude thermosphere above 90 km, the auroral ovals are clearly visible in the MIPAS observations and in the MMMs of all three core model experiments on both days, with higher absolute values on April 9. As discussed before, the MMMs of the three core model experiments agree well with each other here as three of the four chemistry-climate models use AIMOS auroral electrons for all core model experiments. The MMMs of all three core model experiments also agree well with the observations here, both in absolute amounts and in the position and temporal variability of the auroral ovals. In the mid-mesosphere (60–90 km) polewards of 50°, the MIPAS observations show enhanced NO values on both days compared to low- and midlatitudes, with values generally higher during nighttime than during the daytime, and higher on April 9 than on March 30. Of particular note is the night-time enhancement of NO between 60–70°N on March 30, which might be due to enhanced substorm activity starting in the second half of March 30 (see Figure 1). This is not reproduced by the MMMs of any of the core model experiments. On April 9, high-latitude enhancements of mesospheric NO are observed in both hemispheres above 60 km, with the highest values in the night-time Southern hemisphere. These enhancements are reproduced qualitatively by the MMMs of all three core model experiments, with the highest NO values and reasonable quantitative agreement shown for OULU, lowest NO values underestimating observations for APEEP, and intermediate values in the MMMs of AIMOS. These results are consistent with the SCIAMACHY intercomparisons discussed above but again differ from the results of the SOFIE intercomparison provided in Section 3.1. In the lower mesosphere below 60 km, the MIPAS data show large values of enhanced NO of more than 1.5×10^7 cm^{-3} during daytime while nighttime NO concentrations are negligible at these altitudes due to conversion to NO_2. This diurnal cycle is generally well reproduced by the MMMs of all core model experiments, although the NO_x background appears to be overestimated slightly in the lowermost mesosphere.

3.3. Assessment of Differences and Applicability of the Ionization Rate Data-Sets

The Multi-model mean results of the three core model experiments are very similar to each other in the thermosphere above 90 km because three of the four models use auroral electron ionization rates from the same data-set in all core experiments. Below 90 km altitude, the multi-model mean results of the three core experiments differ in accordance with the differences between the ionization rate data-sets, particularly during the storm main and recovery phase. The largest mesospheric NO enhancements are observed for OULU. These NO enhancements also reach furthest down into the mesosphere and persist longest after the storm. The weakest mesospheric NO enhancements are shown for APEEP, with AIMOS intermediate between these extremes. After the recovery phase, AIMOS and APEEP converge and agree reasonably well with each other and after April 14, while in

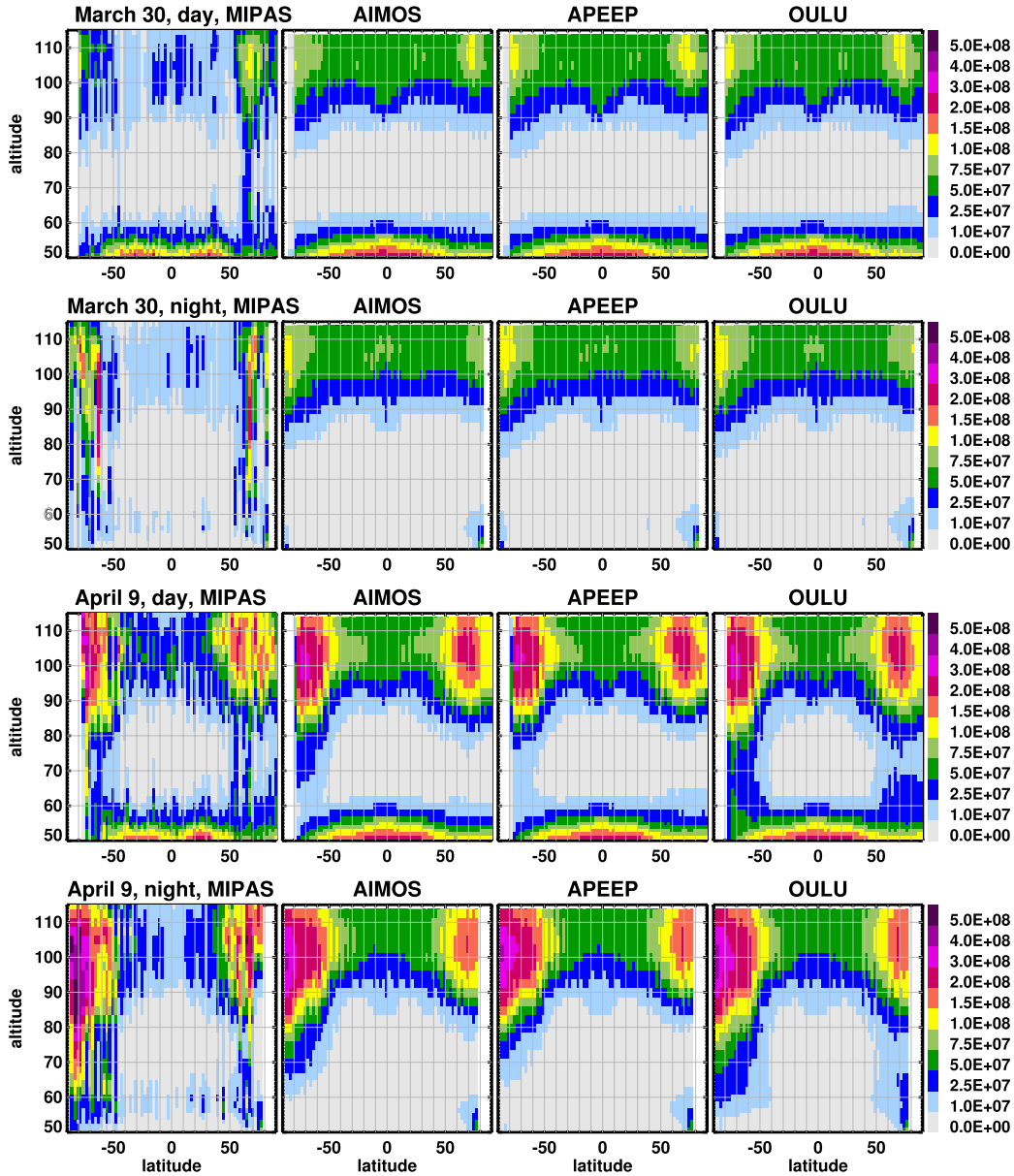

Figure 12. Left: daily mean zonal mean NO density (cm^{-3}) from the MIPAS upper atmosphere mode in 50–115 km on March 30 before the storm, upper two panels, and April 9 in the recovery phase of the storm, bottom two panels. Shown are daytime (sza $\leq 86°$) and nighttime (sza $\geq 94°$) data. Middle to right: multi-model mean results of core model experiments AIMOS, APEEP, and OULU.

OULU, NO densities continue at higher values due to continuing precipitation in the MEE range ≥100 keV until around April 11 (see Figures 4 and 5 of Nesse Tyssøy et al. [2021]).

In the high-latitude uppermost mesosphere and lower thermosphere above 80 km (MIPAS) respectively 85 km (SOFIE, SCIAMACHY), multi-model mean results from all three core model experiments agree well with observations, both quantitatively, and in capturing the spatial and temporal variation. Considering that NO from the individual models varies by up to an order of magnitude here as shown in Section 2.2.6, the good quantitative agreement is likely due to a compensation of different systematic errors of the individual models related to different processes forming and affecting NO as discussed in Section 2.2.7. However, the good agreement in temporal and spatial variability observed in comparison to all three satellite observations above ≈80 km gives confidence

that the auroral electron precipitation and MEE contribution up to energies of about 100 keV are captured well by the different ionization rate data-sets.

In the high-latitude mesosphere at 70–85 km altitude, a more diverse picture presents itself. During the storm main phase (April 6), the MMMs of all three core model experiments agree within error bounds with the SOFIE observations, though the OULU NO densities are higher, and the AIMOS and APEEP NO densities are lower than the mean SOFIE density on this day. Conversely, the MMMs of all three core experiments is lower than the SCIAMACHY data in the high-latitude mesosphere below 80 km (OULU) respectively 85 km (AIMOS, APEEP) on this day, while in 80–85 km, the OULU NO densities are in agreement (Northern hemisphere) or even higher (Southern hemisphere) than the SCIAMACHY NO densities. In the recovery phase (April 9), good agreement is shown in the Southern hemisphere high latitudes between the OULU NO densities and the MIPAS and SCIAMACHY observations in 70–85 km, while the lower AIMOS and APEEP NO densities show good agreement with the SOFIE observations. At high Northern latitudes, reasonable agreement is shown between the OULU NO densities and the MIPAS observations, with lower NO densities in AIMOS and APEEP, while the SCIAMACHY observations are higher than the NO densities from either of the three core model experiments. After the storm period (April 14), the NO densities from AIMOS and APEEP agree well with MIPAS on the SOFIE footprints and with SCIAMACHY around 80 km in high Southern latitudes, while the NO densities from OULU are significantly higher in both cases; however, the MMMs of all three core model experiments are significantly higher than the SOFIE observations in 70–85 km at high Southern latitudes. Below 75 km, the MMMs of all core model experiments show lower NO densities than SCIAMACHY during and after the storm, comparable values between MIPAS and OULU on the SCIAMACHY footprints, while compared with SOFIE and MIPAS on the SOFIE footprint, there is good agreement with AIMOS and APEEP, but significantly higher values in OULU particularly at and below 70 km. Particularly the comparison of the MMMs to SOFIE on the one hand, SCIAMACHY on the other hand after the storm main phase appears contradictory. There are no coinciding observations between SCIAMACHY and SOFIE, and no SCIAMACHY observations below ≈68 km, but MIPAS observations on April 9 and April 14 generally confirm the SCIAMACHY observations of enhanced NO densities throughout the mid-and upper mesosphere above 65 km at high Southern latitudes (see Figure 8). One possible explanation for an underestimation of the model results compared to SCIAMACHY at moderately high latitudes, and simultaneous overestimation compared to SOFIE at very high latitudes, could be related to problems in the vertical and horizontal transport in the models, that is, an overestimation of downward transport through the mesosphere at very high latitudes coupled to an underestimation of horizontal transport to lower latitudes, similar to the impact of vortex strengths discussed after the October 2003 Solar proton event in Funke et al. (2011). Equally, the very high values in the MMMs of OULU on the SOFIE footprint after April 12 below 70 km are more likely due to transport from above 70 km in a strong mesospheric vortex than to continuing precipitation from the high-energy tail of the MEE population. Higher mesospheric NO densities during the storm main and recovery phase (April 6-9) in MIPAS and SCIAMACHY observations compared to SOFIE observations as well as compared to the multi-model mean results could be explained to some extent by the magnetic local time of the ENVISAT overpass during the maximum of MEE precipitation (see Section 2.3). However, this can not explain the differences after the storm period (April 14), and should also be captured by AIMOS which explicitly considers magnetic local time dependence. Considering these qualitative differences, it is not possible to draw a robust conclusion which of the ionization rate data-sets used to provide the best quantitative estimate of the mesospheric NO enhancements during and after the geomagnetic storm below 80 km altitude.

All three satellite instruments show significant NO increases in the mid-mesosphere at and below 70 km altitude in the storm main and the recovery phase (April 7-9). This suggests that electrons with energies from 100 keV to 1 MeV, the high-energy tail of the MEEs, play a role during the storm and in the following days. The satellite NO data differ concerning the strength of this enhancement, possibly suggesting a high variability in the densities of high-latitude NO at this time as seen, for example, in the MIPAS footprint data (Figure 7). As discussed in Section 3.1, it is not possible to unambiguously attribute these enhancements to direct production during the event below 85 km; a significant part of the enhancement may also be due to vertical transport and mixing. MIPAS data above 70 km altitude are not available daily, so an analysis of the day-to-day evolution of NO in the upper mesosphere is not possible based on MIPAS data. However, SCIAMACHY data are available on all days but April 4 in the first half of April 2010, and nine days of SCIAMACHY data are shown in Figure 13. SCIAMACHY data show a slow increase in NO in 70–75 km altitude in early April, with the highest values reached on April 7. While the sharp increase from April 5 to April 6 and from April 6 to April 7 suggest local production

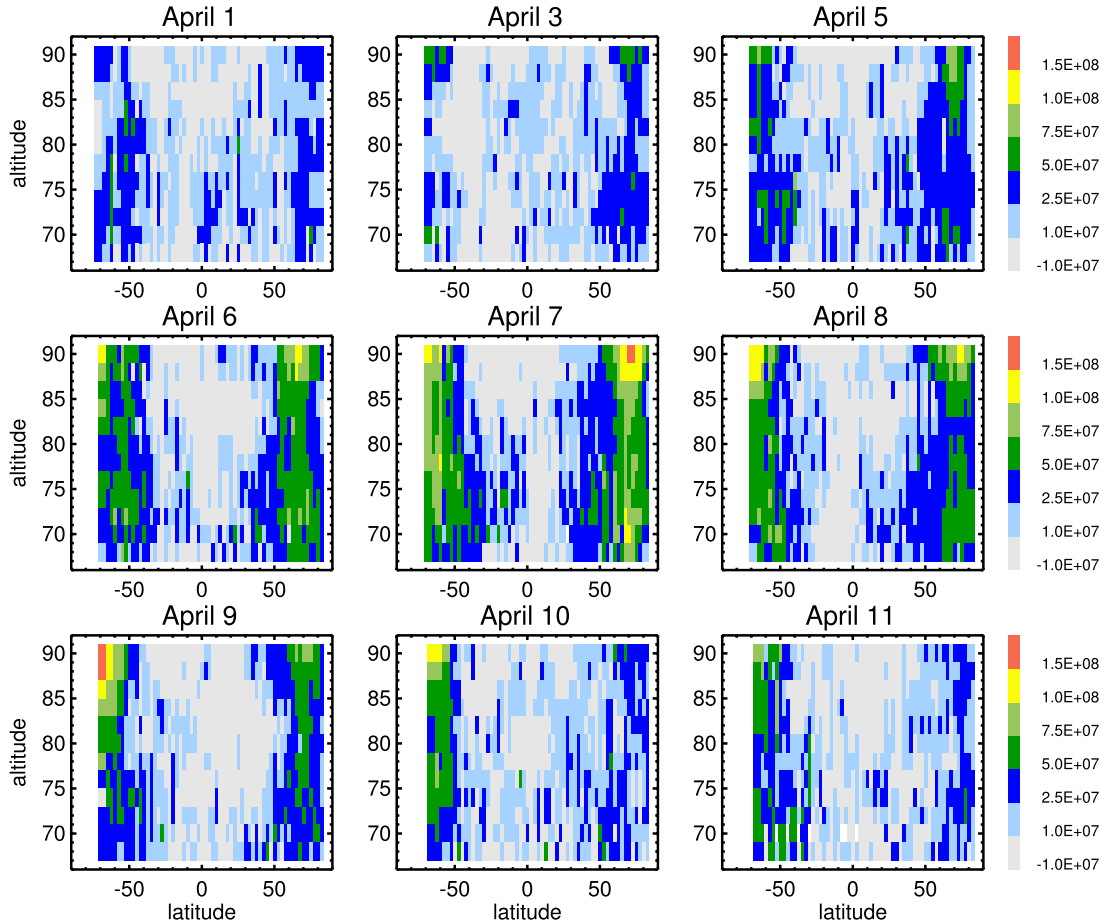

Figure 13. SCIAMACHY NO density (cm^{-3}) on nine days between April 1 and 11 April 2010. The range of the lowest (light gray) contour interval ((−1 – 1) $\times 10^7$ cm^{-3} corresponds to the approximate noise floor of SCIAMACHY.

down to at least 70 km altitude during the storm main phase, a contribution of downward transport from the upper mesosphere above 85 km altitude can not be ruled out either, and the observed high-latitude values at 70–75 km altitude are most likely due to a combination of local production and downward transport at least in the Southern hemisphere. Enhanced values at high Southern latitudes below 70 km altitude on April 8, 11, and 14 (see also Figure 10) suggest continuing downward transport after the event main phase, qualitatively in agreement with SOFIE observations (see Section 3.1). The observed enhancements at and below 70 km altitude are reproduced qualitatively (if not quantitatively) by OULU but not by APEEP which considers the same electron energy range, suggesting highly anisotropic precipitation captured only by the 90° telescope.

In the low- and middle-latitude thermosphere, the multi-model mean results of all three core model experiments consistently overestimate NO compared to observations. This is likely related to the use of the Solomon and Qian (2005) rate parameterization for EUV photoionization in WACCM, HAMMONIA, and EMAC. A similar overestimation of low-latitude thermospheric NO compared to SOFIE observations has already been shown for the TIE-GCM model, which also uses the Solomon and Qian (2005) parameterization (Siskind et al., 2019). Siskind et al. (2019) argue that this overestimation can not be explained by an overestimation of the soft x-ray flux (0.1–30 nm) needed for the photodissociation of N_2, since adapting this would reduce the lower thermospheric electron density which is well constrained by observations. Rather they suggest problems with the kinetic data for the NO formation via $N(^2D)$ or an underestimation of the Lyman-β UV flux (≈103 nm). Since the development of the Solomon and Qian (2005) parameterization, progress has been made in constructing EUV and x-ray spectral variability using observational data not previously available, as for example, used by the FISM2 model (Chamberlin et al., 2018, 2020). Figure 14 shows a comparison of mean spectra of the FISM2 compared to results from the Solomon and Qian (2005) parameterizations during our intercomparison period from March 25 to 10 April

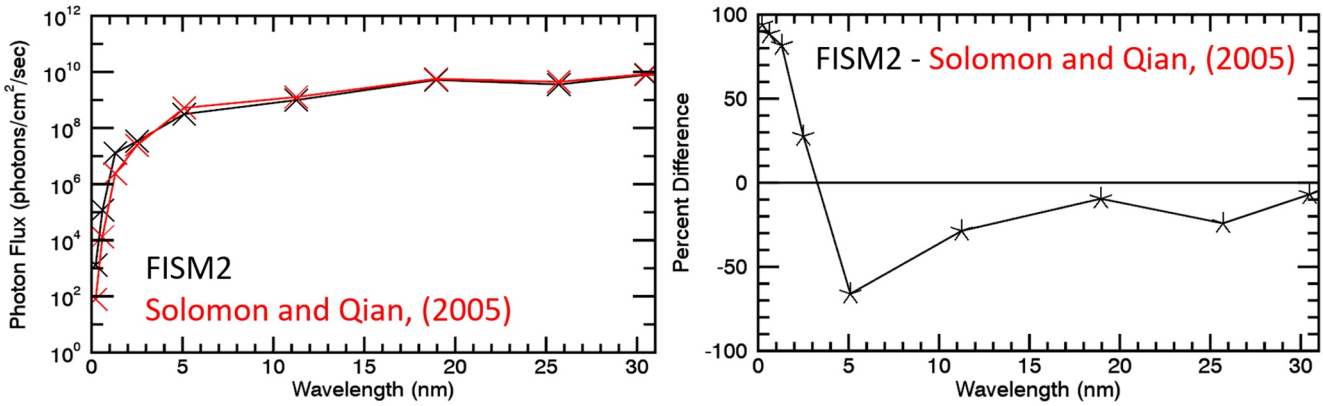

Figure 14. Left: Comparison of average x-ray photon flux for the period March 25 to 10 April 2010, as a function of wavelength (in nm) between FISM2 (black) and the Solomon and Qian (2005) parameterization. Right: difference (%) of FISM2-Solomon and Qian (2005) for the same period.

2010, highlighting higher values in Solomon and Qian (2005) compared to FISM2 in the soft x-ray portion of the spectrum. A concise analysis of this is out of the scope of this paper; however, as photoionization also contributes to high-latitude NO and therefore affects the indirect effect (see, e.g., Figure 6) the issue should be addressed in the near future.

3.4. Contribution of Auroral Electrons and MEE to Hemispheric NO

To assess the impact of auroral and MEE electron precipitation in a more quantitative way, the total hemispheric NO amount is calculated for the multi-model mean results of the model experiments AIMOS, OULU, APEEP, Sens1, and Sens2 from March 16 to April 25 for the altitude range 55–115 km, and additionally 55–90 km for AIMOS and Sens1 only. The contribution of auroral electrons to the total hemispheric NO amount is calculated as the difference between AIMOS and Sens1, the contribution of MEE in the energy range up to 300 keV as the difference between AIMOS and Sens2 (upper panels of Figure 15), the contribution of the ≥300 keV high-energy tail of MEE as the difference between OULU and AIMOS (lower panels of Figure 15). However, the difference between OULU and AIMOS is affected by the different auroral electron data-sets used in WACCM, visible as an offset of ≈0.07 Gmol in both hemispheres during the quiet period before the storm. To account for this, the difference between OULU and AIMOS was separately calculated without the WACCM results. In addition, the difference between OULU and APEEP was calculated. Although these models have the same upper energy limit of 1 MeV, the difference in results below 80 km suggests a contribution from anisotropic precipitation from the high-energy tail during the recovery phase of the storm only captured by the 90° telescope. This comparison, therefore, serves as an additional estimate of an anisotropic high-end tail of MEEs.

The largest contribution to the hemispheric NO budget (0.2–0.9 Gmol) comes from the auroral electrons, though this is mainly restricted to the thermosphere above 90 km; the contribution of auroral electrons to the hemispheric NO budget below 90 km altitude is less than 0.1 Gmol in both hemispheres. The contribution of ≤300 keV MEEs is on average not significant in either hemisphere, likely because it is masked by the internal dynamical variability of the models. All three estimates of the ≥300 keV high-end tail of the MEE distribution show a similar impact on the hemispheric NO budget, with the largest contribution of 0.05–0.15 Gmol during the storm main phase and recovery phase, with enhanced values of more than 0.05 Gmol lasting for several days after the storm. The enhanced values at and shortly after the storm are comparable in magnitude to the contribution of auroral electrons below 90 km. The OULU results are comparable to satellite observations during the storm phase from April 6–10 in 60–80 km, but are significantly higher than the available satellite observations at and below 65 km after April 11 (SOFIE and MIPAS, see Figure 9), so for the post-storm period after April 11, these numbers provide an upper limit only. A step forward in constraining the contribution of the high-energy electrons better could be the inclusion of the POES P6 channel as another source of high-energy electron fluxes, as, for example, provided by the BCSS and MP15 ionization rate data-sets models (see, e.g., Nesse Tyssøy et al. [2021]).

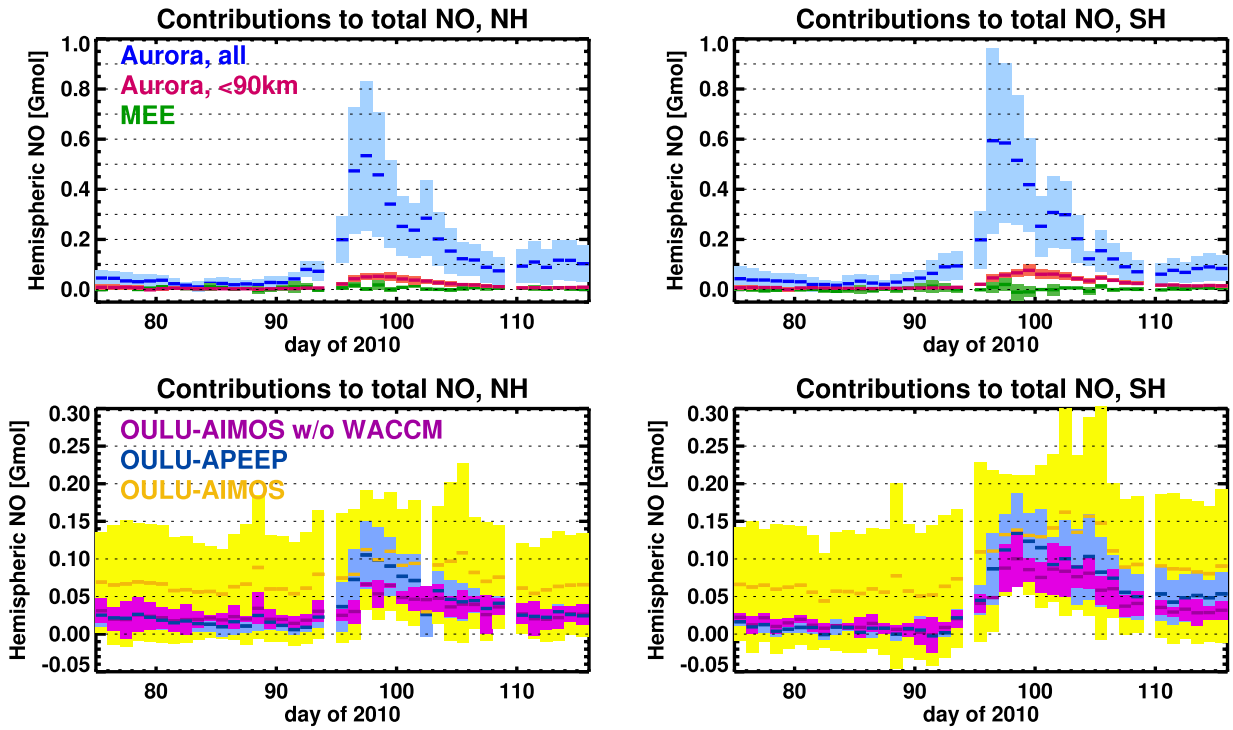

Figure 15. Contributions of electron ionization to the total hemispheric NO budget [Gmol], derived from multi-model mean results. Upper panel: auroral electrons (AIMOS-Sens1, blue) and MEE (AIMOS-Sens2, green). Also provided is the contribution of auroral electrons considering only altitudes ≤90 km (red). Lower panel: different estimates of the high-energy tail of the MEE distribution. Orange: OULU-AIMOS; blue: OULU-APEEP; purple: OULU-AIMOS but without WACCM data. The error range provides the 2σ error of the mean. Left: Northern hemisphere, and right: Southern hemisphere.

4. Conclusions

We compared NO densities from multi-model mean results of three core model experiments using different ionization rate data-sets with satellite observations, as well as NO densities from different chemistry-climate models but using the same electron forcing. Results of these intercomparisons provide a constraint on the validity of the different ionization rate data-sets, but also highlight problems both of the chemistry-climate models used for the model experiments, as well as of the satellite data used for the model-measurement intercomparison.

- In the high-latitude upper mesosphere and lower thermosphere above 80 km altitude, multi-model mean results of NO using different MEE ionization rate data-sets are very similar and agree well with observations there both quantitatively as well as in the spatial and temporal variability. While NO varies by up to an order of magnitude there between models even when using the same electron ionization rates, and the quantitative agreement therefore appears to be due to some extent to compensation of different systematic errors in the different models, the coherence of the spatial and temporal variability with the observations lends confidence that the auroral electron precipitation and ≤100 keV MEE precipitation are captured well by all ionization-rate data-sets
- In the low latitude thermosphere above 90 km altitude, multi-model mean results overestimate NO compared to observations. The large differences between KASIMA on the one hand, and WACCM, HAMMONIA, and EMAC on the other hand suggest that this is related to the NO formation by EUV photoionization, either due to issues with the kinetic reaction rates as suggested by Siskind et al. (2019) or due to the soft x-ray flux ionization. A starting point to address this issue in the future might be the testing of new parameterization of EUV photoionization, sensitivity studies of the kinetic reaction rates and their uncertainties, and simultaneous evaluation against NO and electron density observations
- In the high-latitude mesosphere below 85 km, multi-model mean results using different ionization rate data-sets differ systematically in accordance with differences between the ionization rate data-sets. From the three data-sets studied here, APEEP shows the lowest NO values in the mesosphere, OULU is the highest,

with AIMOS intermediate. Due to the spread of the observations, it is not possible to provide a robust estimate as to which of the ionization rate data-sets perform best below 80 km altitude

- All three observational data-sets agree on a significant NO enhancement during and after the geomagnetic storm at and below 70 km altitude. The temporal evolution of this enhancement as shown in SOFIE and SCIAMACHY data suggests a combination of direct NO production by the high-energy tail of MEE (≥300 keV) with downward transport and mixing from the upper mesosphere. This enhancement is captured by OULU, but not by the other ionization-rate data-sets, indicating anisotropic precipitation observed by the 90° telescope of POES/MEPED. This could contribute up to 0.05–0.15 Gmol of NO to the total hemispheric NOx budget, comparable to the contribution of auroral electrons below 90 km altitude but produced directly in the mid-mesosphere; however, since NO densities from OULU lie at or above the upper edge of the observational spread particularly after the storm period, this estimate based on OULU results can be considered only as an upper limit

To address the issues summarized above, further model experiments over a longer period of time covering several polar winters are needed. To constraint future model experiments better, there is also a clear need for observations of precipitating electron fluxes extending into the high-energy tail of the MEE distribution, as well as of continuing high-quality global observations of NO in the mesosphere and lower thermosphere.

Data Availability Statement

AE and DST data have been provided by World Data Center for Geomagnetism, Kyoto et al. (2015a); World Data Center for Geomagnetism, Kyoto et al. (2015b) at http://wdc.kugi.kyoto-u.ac.jp/. The SML index has been accessed from SuperMAG (Gjerloev, 2012) and we gratefully acknowledge the SuperMAG collaborators (https://supermag.jhuapl.edu/info/). The NOAA/POES data used in this study are available from the National Oceanographic and Atmospheric Administration (https://www.ngdc.noaa.gov/stp/satellite/poes/dataaccess.html). SOFIE level 2 data products are available at http://sofie.gats-inc.com/. SCIAMACHY level 2 NO data are available at https://www.imk-asf/kit.edu/2939.php and at https://www.zenodo.org/record/1009078. MIPAS level 2 NO data are available at https://www.imk-asf.kit.edu/english/308.php. Results of the model experiments summarized in Table 2 from all four chemistry-climate models on the satellite footprints are provided at https://doi.org/10.35097/493 (Sinnhuber et al., 2021).

References

Agostinelli, S., Allison, J., Amako, K., Apostolakis, J., Araujo, H., Arce, P., et al. (2003). Geant4—A simulation toolkit. *Nuclear Instruments and Methods in Physics Research Section A: Accelerators, Spectrometers, Detectors and Associated Equipment*, *506*(3), 250–303. https://doi.org/10.2172/799992

Allen, M., & Frederick, J. E. (1982). Effective photodissociation cross sections for molecular oxygen and nitric oxide in the schumann-runge bands. *Journal of the Atmospheric Sciences*, *39*, 2066–2075. https://doi.org/10.1175/1520-0469(1982)039<2066:epcsfm>2.0.co;2

Andersson, M. E., Verronen, P. T., Marsh, D. R., Päivärinta, S.-M., & Plane, J. M. C. (2016). WACCM-D – improved modeling of nitric acid and active chlorine during energetic particle precipitation. *Journal of Geophysical Research*, *121*, 10,328–10,341. https://doi.org/10.1002/2015JD024173

Arsenovic, P., Rozanov, E., Stenke, A., Funke, B., Wissing, J., Mursula, K., et al. (2016). The influence of middle range energy electrons on atmospheric chemistry and regional climate. *Journal of Atmospheric and Solar-Terrestrial Physics*, *149*, 180–190. https://doi.org/10.1016/j.jastp.2016.04.008

Asikainen, T. (2017). Calibrated and corrected POES/MEPED energetic particle observations. In A. Belehaki, M. Hapgood, & J. Watermann (Eds.), *The ESPAS e-infrastructure: Access to data in near-earth space* (p. 57–69). EDP Open. https://doi.org/10.1051/978-2-7598-1949-2

Asikainen, T. (2019). New homogeneous composite of energetic electron fluxes from POES: 2. Intercalibration of SEM-1 and SEM-2. *Journal of Geophysical Research: Space Physics*, *124*(7), 5761–5782. https://doi.org/10.1029/2019JA026699

Asikainen, T., & Mursula, K. (2011). Recalibration of NOAA/MEPED energetic proton measurements. *Journal of Atmospheric Solar and Terrestrial Physics*, *73*, 335–347. https://doi.org/10.1016/j.jastp.2009.12.011

Asikainen, T., & Mursula, K. (2013). Correcting the NOAA/MEPED energetic electron fluxes for detector efficiency and proton contamination. *Journal of Geophysical Research*, *118*, 6500–6510. https://doi.org/10.1002/jgra.50584

Asikainen, T., Mursula, K., & Maliniemi, V. (2012). Correction of detector noise and recalibration of NOAA/MEPED energetic proton fluxes. *Journal of Geophysical Research*, *117*, a, n. https://doi.org/10.1029/2012JA017593

Asikainen, T., & Ruopsa, M. (2019). New homogeneous composite of energetic electron fluxes from POES satellites: 1. Correction for background noise and orbital drift. *Journal of Geophysical Research: Space Physics*, *124*(2), 1203–1221. https://doi.org/10.1029/2018JA026214

Asikainen, T., Salminen, A., Maliniemi, V., & Mursula, K. (2020). Influence of enhanced planetary wave activity on the polar vortex enhancement related to energetic electron precipitation. *Journal of Geophysical Research: Atmospheres*, *125*, e2019JD032137. https://doi.org/10.1029/2019JD032137

Bacmeister, J. T., Newman, P. A., Gary, B. L., & Chan, K. R. (1994). An algorithm for forecasting mountain wave-related turbulence in the stratosphere. *Weather and Forecasting*, *9*, 241–253. https://doi.org/10.1175/1520-0434(1994)009<0241:aaffmw>2.0.co;2

Acknowledgments

This paper as well as the companion paper are a collaborative effort of the SPARC SOLARIS-HEPPA initiative (solarisheppa.geomar.de) working group five: Medium Energy Electrons (MEE) Model-Measurement intercomparison. T. Asikainen is supported by the Academy of Finland (PROSPECT project no. 321440). H. Nesse Tyssøy is supported by the Norwegian Research Council (NRC) under contracts 223 252, and 302 040. S. Bender and C. Smith-Johnsen are also supported by the Research Council of Norway contract 223 252. B. Funke acknowledges financial support from the Agencia Estatal de Investigación of the Ministerio de Ciencia, Innovación y Universidades through projects ESP2017-87143-R and PID2019-110689RB-I00, as well as the Centre of Excellence "Severo Ochoa" award to the Instituto de Astrofísica de Andalucía (SEV-2017-0709). Work of E. Rozanov on the input data preparation and experimental setup was supported by the German-Russian cooperation project "H-EPIC" funded by the Russian Foundation for Basic Research (RFBR project 20-55-12020). Work of E. Rozanov and T. Sukhodolov on the analysis of results was performed in the SPbSU Ozone Layer and Upper Atmosphere Research Laboratory, which is supported by the Ministry of Science and Higher Education of the Russian Federation under Grant 075-15-2021-583. Work of T. Sukhodolov on the simulation of the atmospheric state with the chemistry-climate model HAMMONIA and analysis of the results was supported by Russian Science Foundation (project No. 21-17-00208). The work of M. E. Szeląg and P. T. Verronen is supported by the Academy of Finland (project No. 335555 ICT-SUNVAC). J.M. Wissing is supported by the German Aerospace Center (DLR; grant no. D/921/67284894). O. Yakovchuk is supported by the German Science Foundation (DFG; grant no. WI4417/2-10381). The EMAC model experiments were performed on the supercomputer ForHLRII funded by the Ministry of Science, Research, and the Arts Baden-Württemberg and by the Federal Ministry of Education and Research.
M. Sinnhuber, B. Funke, J. M. Wissing, and P. T. Verronen would like to thank the International Space Science Institute, Bern, Switzerland for supporting the project "Quantifying Hemispheric Differences in Particle Forcing Effects on Stratospheric Ozone" (Leader: D. R. Marsh).

Barth, C. A., Mankoff, K. D., Bailey, S. M., & Solomon, S. C. (2003). Global observations of nitric oxide in the thermosphere. *Journal of Geophysical Research*, *108*(A1), 1027. https://doi.org/10.1029/2002JA009458

Bender, S., Sinnhuber, M., Burrows, J. P., & Langowski, M. (2017). *Nitric oxide (NO) data set (60–160 km) from SCIAMACHY nominal limb scans*. https://doi.org/10.5281/zenodo.804371

Bender, S., Sinnhuber, M., Burrows, J. P., Langowski, M., Funke, B., & López-Puertas, M. (2013). Retrieval of nitric oxide in the mesosphere and lower thermosphere from SCIAMACHY limb spectra. *Atmospheric Measurement Techniques*, *6*(9), 2521–2531. https://doi.org/10.5194/amt-6-2521-2013

Bender, S., Sinnhuber, M., Langowski, M., & Burrows, J. P. (2017). Retrieval of nitric oxide in the mesosphere from SCIAMACHY nominal limb spectra. *Atmospheric Measurement Techniques*, *10*(1), 209–220. https://doi.org/10.5194/amt-10-209-2017

Bender, S., Sinnhuber, M., von Clarmann, T., Stiller, G., Funke, B., López-Puertas, M., et al. (2015). Comparison of nitric oxide measurements in the mesosphere and lower thermosphere from ACE-FTS, MIPAS, SCIAMACHY, and SMR. *Atmospheric Measurement Techniques*, *8*(10), 4171–4195. https://doi.org/10.5194/amt-8-4171-2015

Bermejo-Pantaleón, D., Funke, B., López-Puertas, M., García-Comas, M., Stiller, G. P., von Clarmann, T., et al. (2011). Global observations of thermospheric temperature and nitric oxide from MIPAS spectra at 5.3 μm. *Journal of Geophysical Research*, *116*. https://doi.org/10.1029/2011JA016752

Bovensmann, H., Burrows, J. P., Buchwitz, M., Frerick, J., Noël, S., Rozanov, V. V., et al. (1999). Sciamachy: Mission objectives and measurement modes. *Journal of the Atmospheric Sciences*, *56*(2), 127–150. https://doi.org/10.1175/1520-0469(1999)056<0127:smoamm>2.0.co;2

Burkholder, J. B., Sander, S. P., Abbatt, J. P. D., Barker, J. R., Huie, R. E., Kolb, C. E., et al. (2015). *Chemical kinetics and photochemical data for use in atmospheric studies*. NASA JPL Technical Report, Evaluation number 18.

Burrows, J. P., Hölzle, E., Goede, A. P. H., Visser, H., & Fricke, W. (1995). Sciamachy – Scanning imaging absorption spectrometer for atmospheric chartography. *Acta Astronautica*, *35*(7), 445–451. https://doi.org/10.1016/0094-5765(94)00278-T

Chamberlin, P. C., Eparvier, F. G., Knoer, V., Leise, H., Pankratz, A., Snow, M., et al. (2020). The flare irradiance spectral model-version 2 (FISM2). *Space Weather*, *18*, e2020SW002588. https://doi.org/10.1029/2020SW002588

Chamberlin, P. C., Woods, T. N., Didkovsky, L., Eparvier, F. G., Jones, A. R., Machol, J. L., et al. (2018). Solar ultraviolet irradiance observations of the solar flares during the intense september 2017 storm period. *Space Weather*, *16*, 1470, 1487. https://doi.org/10.1029/2018SW001866

Dietmüller, S., Jöckel, P., Tost, H., Kunze, M., Gellhorn, C., Brinkop, S., et al. (2016). A new radiation infrastructure for the Modular Earth Submodel System (MESSy, based on version 2.51). *Geoscientific Model Development*, *9*, 2209–2222. https://doi.org/10.5194/gmd-9-2209-2016

Dobbin, A. L., & Aylward, A. D. (2008). A three-dimensional modelling study of the processes leading to mid latitude nitric oxide increases in the lower thermosphere following periods of high geomagnetic activity. *Advances in Space Research*, *42*, 1576–1585. https://doi.org/10.1016/j.asr.2008.03.004

Egorova, T., Rozanov, E., Orsolini, Y., Shapiro, A., Calisto, M., Peter, T., & Schmutz, W. (2011). The atmospheric effects of october 2003 solar proton event simulated with the chemistry–climate model SOCOL using complete and parameterized ion chemistry. *JASTP*, *73*, 356–365. https://doi.org/10.1016/j.jastp.2010.01.009

Emmons, L. K., Walters, S., Hess, P. G., Lamarque, J., Pfister, G. G., Fillmore, D., et al. (2010). Description and evaluation of the model for ozone and related chemical tracers, version 4 (mozart-4). *Geoscientific Model Development*, *3*, 43–67. https://doi.org/10.5194/gmd-3-43-2010

Evans, D. S., & Greer, M. S. (2006). *Polar orbiting Environmental satellite Space Environment Monitor - 2, instrument descriptions and Archive data Documentation [computer software manual]*. NOAA Space Environ. Lab, (Version 2.0).

Fang, X., Randall, C. E., Lummerzheim, D., Wang, W., Lu, G., Solomon, S. C., & Frahm, R. A. (2010). Parameterization of monoenergetic electron impact ionization. *Geophysical Research Letters*, *37*(22). https://doi.org/10.1029/2010GL045406

Fischer, H., Birk, M., Blom, C., Carli, B., Carlotti, M., von Clarmann, T., et al. (2008). Mipas: An instrument for atmospheric and climate research. *Atmospheric Chemistry and Physics*, *8*, 2151–2188. https://doi.org/10.5194/acp-8-2151-2008

Funke, B., Baumgaertner, A., Calisto, M., Egorova, T., Jackman, C. H., Kieser, J., et al. 2011). Composition changes after the Halloween solar proton event: The high energy particle precipitation in the atmosphere (HEPPA) model versus MIPAS data study. *Atmospheric Chemistry and Physics*, *11*, 9089–9139. https://doi.org/10.5194/acp-11-9089-2011

Funke, B., López-Puertas, M., Stiller, G., & von Clarmann, T. (2014). Mesospheric and stratospheric NOy produced by energetic particle precipitation during 2002–2012. *Journal of Geophysical Research: Atmosphere*, *119*, 4429–4446. https://doi.org/10.1002/2013JD021404

Gettelman, A., Mills, M. J., Kinnison, R. R. D. E., Garcia Smith, A. K., Marsh, D. R., Tilmes, S., et al. (2019). The whole atmosphere community climate model version 6 (WACCM6). *Journal of Geophysical Research: Atmosphere*, *124*, 12380–12403. https://doi.org/10.1029/2019JD030943

Gjerloev, J. W. (2012). The SuperMAG data processing technique. *Journal of Geophysical Research: Space Physics*, *117*(A9). https://doi.org/10.1029/2012JA017683

Gordley, L. L., Hervig, M. E., Fish III, J. M. C., Bailey, S., Cook, J., Hansen, S., et al. (2009). The Solar Occultation For Ice Experiment. *Journal of Atmospheric and Solar-Terrestrial Physics*, *71*, 300–315. https://doi.org/10.1016/j.jastp.2008.07.012

Hervig, M., Marshall, B., Bailey, S., Siskind, D., Russell III, J., Bardeen, C., et al. (2019). Validation of Solar Occultation For Ice Experiment (SOFIE) nitric oxide measurements. *Atmospheric Measurement Techniques*, *12*, 3111–3121. https://doi.org/10.5194/amt-12-3111-2019

Hines, C. (1997). Doppler-spread parameterization of gravity-wave momentum deposition in the middle atmosphere. part 1: Basic formulation. *Journal of Atmospheric and Solar-Terrestrial Physics*, *59*, 371–386. https://doi.org/10.1016/s1364-6826(96)00079-x

Hong, S.-S., & Lindzen, R. (1976). Solar semidiurnal tide in the thermosphere. *Journal of the Atmospheric Sciences*, *33*, 135–153. https://doi.org/10.1175/1520-0469(1976)033<0135:sstitt>2.0.co;2

Jackman, C. H., Deland, M. T., Labow, G. J., Fleming, E. L., Weisenstein, D. K., Ko, M. K. W., et al. (2005). Neutral atmospheric influences of the solar proton events in October-November 2003. *Journal of Geophysical Research*, *110*, A09S27. https://doi.org/10.1029/2004JA010888

Jackman, C. H., Marsh, D. R., Vitt, F. M., Roble, R. G., Randall, C. E., Bernath, P. F., et al. (2011). Northern Hemisphere atmospheric influence of the solar proton events and ground level enhancement in January 2005. *Atmospheric Chemistry and Physics*, *11*, 6153–6166. https://doi.org/10.5194/acp-11-6153-2011

Jackman, C. H., McPeters, R. D., Labow, G. J., & Fleming, E. L., Praderas, C. J., Russell, J. M. (2001). Northern hemisphere atmospheric effects due to the july 2000 solar proton event. *Geophysical Research Letters*, *28*, 2883–2886. https://doi.org/10.1029/2001gl013221

Joeckel, P., Kerkweg, A., Pozzer, A., Sander, R., Tost, H., Rieder, H., et al. (2010). Development cycle 2 of the Modular Earth Submodel System (MESSy2). *Geoscientific Model Development*, *3*, 717–752. https://doi.org/10.5194/gmd-3-717-2010

Kieser, J., Schmidt, H., Wissing, J. M., & Kallenrode, M. B. (2009). The influence of precipitating solar and magnetospheric particles on the entire atmosphere - simulations with HAMMONIA. In *EGU general assembly conference abstracts* (p. 5718).

Kinnison, D. E., Brasseur, G. P., Walters, S., Garcia, R. R., Marsh, D. A., Sassi, F., et al. (2007). Sensitivity of chemical tracers to meteorological parameters in the MOZART-3 chemical transport model. *Journal of Geophysical Research*, *112*, D20302. https://doi.org/10.1029/2006JD007879

Kouker, W., Langbein, I., Reddmann, T., & Ruhnke, R. (1999). *The Karlsruhe SImulation model of the Middle Atmosphere version 2, Wiss*. Ber. FZKA 6278, Forsch. Karlsruhe.

Kunze, M., Godolt, M., Langematz, U., Grenfell, J., Hamann-Reinus, A., & Rauer, H. (2014). Investigating the early earth faint your sun problem with a general circulation model. *Planetary and Space Science*, *98*, 77–92. https://doi.org/10.1016/j.pss.2013.09.011

Lamarque, J., Emmons, L. K., Hess, P. G., Kinnison, D. E., Tilmes, S., Vitt, F., et al. (2012). Cam-chem: Description and evaluation of interactive atmospheric chemistry in the community earth system model. *Geoscientific Model Development*, *5*, 369–411. https://doi.org/10.5194/gmd-5-369-2012

Lott, F., & Miller, M. J. (1997). A new subgrid-scale orographic drag parametrization: Its formulation and testing. *Quarterly Journal of the Royal Meteorological Society*, *123*(537), 101–127. https://doi.org/10.1002/qj.49712353704

Maliniemi, V., Asikainen, T., & Mursula, K. (2014). Spatial distribution of northern hemisphere winter temperatures during different phases of the solar cycle. *Journal of Geophysical Research: Atmospheres*, *119*(16), 9752–9764. https://doi.org/10.1002/2013JD021343

Maliniemi, V., Asikainen, T., Salminen, A., & Mursula, K. (2019). Assessing north atlantic winter climate response to geomagnetic activity and solar irradiance variability. *Quarterly Journal of the Royal Meteorological Society*, *145*(725), 3780–3789. https://doi.org/10.1002/qj.3657

Marsh, D., Mills, M., Kinnison, D., Lamarque, J.-F., Calvo, N., & Polvani, L. (2013). Climate change from 1850 to 2005 simulated in CESM1(WACCM). *Journal of Climate*, *26*, 7372–7391. https://doi.org/10.1175/JCLI-D-12-00558.1

Marsh, D. R., Garcia, R. R., Kinnison, D. E., Boville, B. A., Sassi, F., Solomon, S. C., & Matthes, K. (2007). Modeling the whole atmosphere response to solar cycle changes in radiative and geomagnetic forcing. *Journal of Geophysical Research*, *112*, D23306. https://doi.org/10.1029/2006JD008306

Marsh, D. R., Solomon, S. C., & Reynolds, A. E. (2004). Empirical model of nitric oxide in the lower thermosphere. *Journal of Geophysical Research*, *109*, A07301. https://doi.org/10.1029/2003JA010199

Matthes, K., Funke, B., Anderson, M., Barnard, L., Beer, J., Charbonneau, P., et al. (2017). Solar forcing for CMIP-6. *Geoscientific Model Development*, *10*, 2247–2302. https://doi.org/10.5194/gmd-10-2247-2017

Meraner, K., Schmidt, H., Manzini, E., Funke, B., & Gardini, A. (2016). Sensitivity of simulated mesospheric transport of nitrogen oxides to parameterized gravity waves. *Journal of Geophysical Research*, *121*(20), 12,045–12,061. https://doi.org/10.1002/2016JD025012

Minschwaner, K., & Siskind, D. E. (1993). A new calculation of nitric oxide photolysis in the stratosphere, mesosphere, and lower thermosphere. *Journal of Geophysical Research*, *98*(D11), 20,401–20,412. https://doi.org/10.1029/93JD02007

Mironova, I., Aplin, K., Arnold, F., Bazilevskaya, G., Harrison, R., Krivolutsky, A., et al. (2015). Energetic particle influence on the earth's atmosphere. *Space Science Reviews*, *194*, 1–96. https://doi.org/10.1007/s11214-015-0185-4

Mironova, I. A., Artamonov, A. A., Bazilevskaya, G. A., Rozanov, E. V., Kovaltsov, G. A., Makhmutov, V. S., et al. (2019). Ionization of the polar atmosphere by energetic electron precipitation retrieved from balloon measurements. *Geophysical Research Letters*, *46*(2), 990–996. https://doi.org/10.1029/2018GL079421

Molod, A., Takacs, L., Suarez, M., & Bacmeister, J. (2015). Development of the GEOS-5 atmospheric general circulation model: Evolution from MERRA to MERRA2. *Geoscientific Model Development*, *8*, 1339–1356. https://doi.org/10.5194/gmd-8-1339-2015

Nesse Tyssøy, H., Haderlein, A., Sandanger, M., & Stadsnes, J. (2019). Intercomparison fo the POES/MEPED loss cone electron fluxes with the CMIP6 parametrization. *Journal of Geophysical Research*, *124*, 628–642. https://doi.org/10.1029/2018JA025745

Nesse Tyssøy, H., Sinnhuber, M., Asikainen, T., Bender, S., Clilverd, M. A., Funke, B., et al. (2021). HEPPA III intercomparison experiment on electron precipitation impacts: 1. Estimated ionization rates during a geomagnetic active period in April 2010. *Journal of Geophysical Research: Space Physics*, *127*, e2021JA029128. https://doi.org/10.1029/2021JA029128

Newell, P. T., & Gjerloev, J. W. (2011a). Evaluation of SuperMAG auroral electrojet indices as indicators of substorms and auroral power. *Journal of Geophysical Research*, *116*(A15, a, n), A12211. https://doi.org/10.1029/2011JA016779

Newell, P. T., & Gjerloev, J. W. (2011b). Substorm and magnetosphere characteristic scales inferred from the SuperMAG auroral electrojet indices. *Journal of Geophysical Research*, *116*(A15), A12232. https://doi.org/10.1029/2011JA016936

Nissen, K. M., Matthes, K., Langematz, U., & Mayer, B. (2007). Towards a better representation of the solar cycle in general circulation models. *Atmospheric Chemistry and Physics*, *7*, 5391–5400. https://doi.org/10.5194/acp-7-5391-2007

O'Brien, T. P., & Moldwin, M. B. (2003). Empirical plasmapause models from magnetic indices. *Geophysical Research Letters*, *30*(4), 1152. https://doi.org/10.1029/2002GL016007

Pettit, J. M., Randall, C. E., Peck, E. D., Marsh, D. R., van de Kamp, M., Fang, X., et al. (2019). Atmospheric effects of >30-kev energetic electron precipitation in the southern hemisphere winter during 2003. *Journal of Geophysical Research: Space Physics*, *124*(10), 8138–8153. https://doi.org/10.1029/2019JA026868

Picone, J. M., Hedin, A. E., Drob, D. P., & Aikin, A. C. (2002). Nrlmsise-00 empirical model of the atmosphere: Statistical comparisons and scientific issues. *Journal of Geophysical Research - A: Space Physics*, *107*(A12, 15, 1), 1468. https://doi.org/10.1029/2002JA009430

Porter, H. S., Jackman, C. H., & Green, A. E. S. (1976). Efficiences for the production of atomic nitrogen and oxygen by relativistic proton impact in air. *The Journal of Chemical Physics*, *65*, 154–167. https://doi.org/10.1063/1.432812

Richards, P. G. (2004). On the increases in nitric oxide density at midlatitudes during ionospheric storms. *Journal of Geophysical Research*, *109*, A06304. https://doi.org/10.1029/2003JA010110

Richter, J. H., Sassi, F., & Garcia, R. R. (2010). Toward a physically based gravity wave source parameterization in a general circulation model. *Journal of the Atmospheric Sciences*, *67*(1), 136–156. https://doi.org/10.1175/2009JAS3112.1

Roble, R. G., & Ridley, E. C. (1994). A thermosphere-ionosphere-mesosphere-electrodynamics general circulation model (time-gcm): Equinox solar cycle minimum simulations (30–500 km). *Geophysical Research Letters*, *21*, 417–420. https://doi.org/10.1029/93GL03391

Roeckner, E., Bäuml, G., Bonaventura, L., Brokopf, R., Esch, M., Giorgetta, M., et al. (2003). *The Atmospheric General Circulation Model ECHAM5, Part I. Techn. Ber*. No. 349, Max-Planck-Institut fur Meteorologie, 349.

Roeckner, E., Brokopf, R., Esch, M., Giorgetta, M., Hagemann, S., Kornblueh, L., et al. (2006). Sensitivity of simulated climate to horizontal and vertical resolution in the ECHAM5 atmosphere model. *Journal of Climate*, *19*, 3771–3791. https://doi.org/10.1175/jcli3824.1

Sander, R., Abbatt, J., Barker, J., Burkholder, J., Friedl, R., Golden, D., et al. (2011). *Chemical kinetics and photochemical data for use in atmospheric studies. Jet Propulcion Laboratory*, Evaluation No. 17, JPL Publication 10–6, California Institute of Technology.

Sander, R., Baumgaertner, A., Gromov, S., Harder, H., Jöckel, P., Kerkweg, A., et al. (2011). The atmospheric chemistry box model CAABA/MECCA-3.0. *Geoscientific Model Development*, *4*, 373–380. https://doi.org/10.5194/gmd-4-373-2011

Sander, R., Joeckel, P., Kirner, O., Kunert, A., Landgraf, J., & Pozzer, A. (2014). The photolysis module Jval-14, compatible with the MESSy standard, and the Jval preprocessor (Jvpp). *Geoscientific Model Development*, *7*, 2563–2662. https://doi.org/10.5194/gmd-7-2653-2014

Schmidt, H., Brasseur, G. P., Charron, M., Manzini, E., Giorgetta, M. A., Diehl, T., et al. (2006). The HAMMONIA chemistry climate model: Sensitivity of the mesopause region to the 11-year solar cycle and CO2 Doubling. *Journal of Climate*, *19*(16, 3903, 3931), 3903. https://doi.org/10.1175/JCLI3829.1

Schröter, J., Heber, B., Steinhilber, F., & Kallenrode, M. (2006). Energetic particles in the atmosphere: A monte-carlo simulation. *Advances in Space Research*, *37*(8), 1597–1601. https://doi.org/10.1016/j.asr.2005.05.085

Scinocca, J. F., & McFarlane, N. A. (2000). The parametrization of drag induced by stratified flow over anisotropic orography. *Quarterly Journal of the Royal Meteorological Society*, *126*, 2353–2393. https://doi.org/10.1002/qj.49712656802

Seppälä, A., Randall, C. E., Clilverd, M. A., Rozanov, E., & Rodger, C. J. (2009). Geomagnetic activity and polar surface air temperature variability. *Journal of Geophysical Research*, *114*, A10312. https://doi.org/10.1029/2008JA014029

Sinnhuber, M., Berger, U., Funke, B., Nieder, H., Reddmann, T., Stiller, G., et al. (2018). NOy production, ozone loss and changes in net radiative heating due to energetic particle precipitation in 2002-2010. *Atmospheric Chemistry and Physics*, *18*, 1115–1147. https://doi.org/10.5194/acp-18-1115-2018

Sinnhuber, M., Friederich, F., Bender, S., & Burrows, J. P. (2016). The response of mesospheric NO to geomagnetic forcing in 2002–2012 as seen by sciamachy. *Journal of Geophysical Research*, *121*, 3603–3620. https://doi.org/10.1002/2015JA022284

Sinnhuber, M., & Funke, B. (2019). Energetic electron precipitation into the atmosphere. In A. Jaynes (Ed.), *The dynamic loss of Earth's radiation belts: From Loss in the Magnetosphere to Particle Precipitation in the Atmosphere* (pp. 279–321). Elsevier. https://doi.org/10.1016/B978-0-12-813371-2.00009-3

Sinnhuber, M., Nieder, H., & Wieters, N. (2012). Energetic particle precipitation and the chemistry of the mesosphere/lower thermosphere. *Surveys in Geophysics*, *33*, 1281–1334. https://doi.org/10.1007/s10712-012-9201-3

Sinnhuber, M., Smith-Johnsen, C., Nesse Tyssoy, H., Reddmann, T., Verronen, P. T., Rozanov, E., et al. (2021). *Chemistry-climate model results of nitric oxide for the Heppa III intercomparison experiment on electron precipitation impacts*. https://doi.org/10.35097/493

Siskind, D. E., McArthur, J. J., Drob, D. P., McCormack, J. P., Hervig, M. E., Marsh, D. R., et al. (2019). On the relative roles of dynamics and chemistry governing the abundance and diurnal variation of low-latitude thermospheric nitric oxide. *Annals of Geophysics*, *37*, 37–48. https://doi.org/10.5194/angeo-37-37-2019

Smith-Johnsen, C., Marsh, D., Orsolini, Y., Nesse Tyssøy, H., Hendrickx, K., Sandanger, M., et al. (2018). Nitric oxide response to the April 2010 electron precipitation event: Using WACCM and WACCM-D with and without medium-energy electrons. *Journal of Geophysical Research*, *123*, 5232–5245. https://doi.org/10.1029/2018JA025418

Smith-Johnsen, C., Nesse Tyssøy, H., Hendrickx, K., Orsolini, Y., Kumar, G., GlesnesØdegard, L.-K., et al. (2017). Direct and indirect electron precipitation effect on nitric oxide in the polar middle atmosphere using a full-range energy spectrum. *Journal of Geophysical Research: Space Physics*, *122*, 8679–8693. https://doi.org/10.1002/2017JA024364

Solomon, S. C., & Qian, L. (2005). Solar extreme-ultraviolet irradiance for general circulation models. *Journal of Geophysical Research*, *110*, A10306. https://doi.org/10.1029/2005JA011160

Tilmes, S., Lamarque, J., Emmons, L. K., Kinnison, D. E., Marsh, D., Garcia, R. R., et al. (2016). Representation of the community earth system model (CeSM1) CAM4-CHEM within the chemistry-climate model initiative (CCMI). *Geoscientific Model Development*, *9*, 1853–1890. https://doi.org/10.5194/gmd-9-1853-2016

van de Kamp, M., Seppälä, A., Clilverd, M. A., Rodger, C. J., Verronen, P. T., & Whittaker, I. C. (2016). A model providing long-term data sets of energetic electron precipitation during geomagnetic storms. *Journal of Geophysical Research Atmosphere*, *121*, 520, 12. https://doi.org/10.1002/2015JD024212

Verronen, P. T., Andersson, M. E., Marsh, D. R., Kovács, T., & Plane, J. M. C. (2016). WACCM-D – whole atmosphere community climate model with D-region ion chemistry. *Journal of Advances in Modeling Earth Systems*, *8*, 954–975. https://doi.org/10.1002/2015MS000592

Verronen, P. T., & Lehmann, R. (2013). Analysis and parameterisation of ionic reactions affecting middle atmospheric HO_x and NO_y during solar proton events. *Annals of Geophysics*, *31*, 909–956. https://doi.org/10.5194/angeo-31-909-2013

Verronen, P. T., Seppälä, A., Clilverd, M. A., Rodger, C. J., Kyrölä, E., Enell, C.-F., et al. (2005). Diurnal variation of ozone depletion during the October–November 2003 solar proton events. *Journal of Geophysical Research*, *110*, A09S32. https://doi.org/10.1029/2004JA010932

Winkler, H., Sinnhuber, M., Notholt, J., Kallenrode, M.-B., Steinhilber, F., Vogt, J., et al. (2008). Modeling impacts of geomagnetic field variations on middle atmospheric ozone responses to solar proton events on long timescales. *Journal of Geophysical Research*, *113*, D02302. https://doi.org/10.1029/2007JD008574

Wissing, J. M., & Kallenrode, M.-B. (2009). Atmospheric ionization module osnabrück (aimos): A 3-d model to determine atmospheric ionization by energetic charged particles from different populations. *Journal of Geophysical Research: Space Physics*, *114*(A6). https://doi.org/10.1029/2008JA013884

Wissing, J. M., Nieder, H., Yakovchouk, O. S., & Sinnhuber, M. (2016). Particle precipitation: How the spectrum fit impacts atmospheric chemistry. *Journal of Atmospheric and Solar-Terrestrial Physics*, *149*, 191–206. https://doi.org/10.1016/j.jastp.2016.04.007

WMO. (2018). *Scientific assessment of ozone depletion: 2018*. World Meteorological Organization Report. Retrieved from https://csl.noaa.gov/assessments/ozone/2018/

World Data Center for Geomagnetism, Kyoto, Nose, M., Iyemori, T., Sugiura, M., & Kamei, T. (2015a). *Geomagnetic AE index*. https://doi.org/10.17593/15031-54800

World Data Center for Geomagnetism, Kyoto, Nose, M., Iyemori, T., Sugiura, M., & Kamei, T. (2015b). *Geomagnetic DST index*. https://doi.org/10.17593/14515-74000

Yakovchuk, O., & Wissing, J. M. (2019). Magnetic local time asymmetries in precipitating electron and proton populations with and without substorm activity. *Annales Geophysicae*, *37*(6), 1063–1077. https://doi.org/10.5194/angeo-37-1063-2019

Zhang, Y., & Paxton, L. (2008). An empirical kp-dependent global auroral model based on TIMED/GUVI FUV data. *Journal of Atmospheric and Solar-Terrestrial Physics*, *70*(8), 1231–1242. https://doi.org/10.1016/j.jastp.2008.03.008